

# 1 Soil smoldering in temperate forests : A neglected contributor to fire 2 carbon emissions revealed by atmospheric mixing ratios

3 Lilian Vallet<sup>1,2</sup>, Charbel Abdallah<sup>3</sup>, Thomas Lauvaux<sup>3</sup>, Lilian Joly<sup>3</sup>, Michel Ramonet<sup>4</sup>, Philippe Ciais<sup>4</sup>,  
4 Morgan Lopez<sup>4</sup>, Irène Xueref-Remy<sup>5</sup>, Florent Mouillot<sup>1</sup>

5 <sup>1</sup> Centre d'Ecologie Fonctionnelle et Evolutive CEFE, UMR5175, CNRS, Université de Montpellier, Université Paul-Valéry  
6 Montpellier, EPHE, 1919 Route de Mende, 34293 Montpellier Cedex 5, France

7 <sup>2</sup> French Environment and Energy Management Agency, 20 avenue du Grésillé BP 90406 49004 Angers CEDEX 01, France

8 <sup>2</sup> Groupe de Spectrométrie Moléculaire et Atmosphérique (GSMA), Université de Reims-Champagne Ardenne, UMR CNRS  
9 7331, Reims, France

10 <sup>3</sup> Laboratoire des Sciences du Climat et de l'Environnement (LSCE), IPSL, CEA-CNRS-UVSQ, Unmagiversité Paris-Saclay,  
11 91191 Gif sur Yvette Cedex, France

12 <sup>4</sup> Institut Méditerranéen de Biodiversité et Ecologie Marine et Continentale (IMBE), Aix-Marseille Université, CNRS, Institut  
13 de Recherche pour le Développement (IRD), Avignon Université, 13290 Aix-en-Provence, France

14 *Correspondence to:* Lilian VALLET ([lilian.vallet@cefe.cnrs.fr](mailto:lilian.vallet@cefe.cnrs.fr))

15 **Abstract.** Fire is considered as an essential climate variable, emitting greenhouse gases in the combustion process. Current  
16 global assessments of fire emissions traditionally rely on coarse remotely-sensed burned area data, along with biome-specific  
17 combustion completeness and emission factors. However, large uncertainties persist regarding burned areas, biomass affected,  
18 and emission factors. Recent increases in resolution have improved previous estimates of burned areas and aboveground  
19 biomass, while increasing the information content used to derive emission factors, complemented by airborne sensors deployed  
20 in the Tropics. To date, temperate forests, characterized by a lower fire incidence and stricter aerial surveillance restrictions  
21 near wildfires, have received less attention. In this study, we leveraged the distinctive fire season of 2022, which impacted  
22 Western European temperate forests, to investigate fire emissions monitored by the atmospheric tower network. We examined  
23 the role of soil smoldering combustion responsible for higher carbon emissions, locally reported by firefighters but not  
24 accounted for in temperate fire emission budgets. We assessed the CO/CO<sub>2</sub> ratio released by major fires in the Mediterranean,  
25 Atlantic pine, and Atlantic temperate forests of France. Our findings revealed low Modified Combustion Efficiency (MCE)  
26 for the two Atlantic temperate regions, supporting the assumption of heavy smoldering combustion. This type of combustion  
27 was associated with specific fire characteristics, such as long-lasting thermal fire signals, and affected ecosystems  
28 encompassing needle leaf species, peatlands, and superficial lignite deposits in the soils. Thanks to high-resolution data  
29 (approximately 10 meters) on burned areas, tree biomass, peatlands, and soil organic matter, we proposed a revised combustion  
30 emission framework consistent with the observed MCEs. Our estimates revealed that 6.15 MtCO<sub>2</sub> ( $\pm 2.65$ ) were emitted, with  
31 belowground stock accounting for 51.75% ( $\pm 16.05$ ). Additionally, we calculated a total emission of 1.14 MtCO ( $\pm 0.61$ ), with  
32 84.85% ( $\pm 3.75$ ) originating from belowground combustion. As a result, the carbon emissions from the 2022 fires in France  
33 amounted to 7.95 MteqCO<sub>2</sub> ( $\pm 3.62$ ). These values exceed by 2-fold the GFAS estimates for the country, reaching 4.18  
34 MteqCO<sub>2</sub> (CO and CO<sub>2</sub>). Fires represent 1.97% ( $\pm 0.89$ ) of the country's annual carbon footprint, corresponding to a reduction  
35 of 30 % of the forest carbon sink this year. Consequently, we conclude that current European fire emissions estimates should  
36 be revised to account for soil combustion in temperate forests. We also recommend the use of atmospheric mixing ratios as an  
37 effective monitoring system of prolonged soil fires that have the potential to reignite in the following weeks.

## 38 **1 Introduction**

39 Wildfires recurrently affect European forests, particularly in the southern regions characterized by a Mediterranean climate  
40 and northern boreal regions (European Commission. Joint Research Centre., 2023). In contrast, fire activity is significantly  
41 lower in wetter temperate and alpine forests, resulting in relatively less interest and fewer impact assessment studies (Zin et  
42 al., 2022). However, this established paradigm of wildfire distribution in Europe may undergo substantial modifications as a  
43 result of climate change (Wu et al., 2015). Climate change has the potential to intensify the already recurring fires in the  
44 Mediterranean basin under more frequent heat waves (Ruffault et al., 2020) and reshape pyroregions (Galizia et al., 2023). In  
45 particular, the year 2022 exhibited highly distinctive fire events in the western Mediterranean basin and experienced unusual  
46 heat waves and subsequent forest fires in the temperate forests across northern France, Germany, the Czech Republic, and the  
47 UK (Rodrigues et al., 2023). These atypical fire events could potentially serve as a preview of future fire distribution, posing  
48 a significant risk to temperate forests (Galizia et al., 2023).

49 However, limited information is currently available to assess the impacts of this atypical fire distribution, particularly  
50 concerning carbon emissions into the atmosphere. The gaps in our current understanding of these fires are mainly due to the  
51 rare occurrence of such fire distribution within European fire regimes, also impaired by the lack of remote sensing  
52 measurements until recently. In a preliminary investigation of fire effects on temperate forests, Vallet et al. (2023) focused on  
53 the 2022 fire season as a unique study case. They identified an increased loss of wood biomass in old-growth temperate forests,  
54 less affected by fires in the last decades compared to the Mediterranean forests which are mostly affected in their early stage  
55 of forest succession as shrublands. Nevertheless, the impacts of fire on biomass combustion and the resulting carbon emission  
56 have not been assessed. Moreover, the combustion of soil, often disregarded in fire-prone Mediterranean ecosystems, remains  
57 under-studied due to their thin litter layer and low soil organic content resulting from mild temperatures and high  
58 decomposition rates (Jonard et al., 2017; De Vos et al., 2015). The impact of fires on soil carbon stocks is only extensively  
59 considered in boreal forests and tropical peatlands where fire incidence is higher (Astiani et al., 2018; Asbjornsen et al., 2005).  
60 However, temperate forests still harbor significant burnable soil carbon pools and peatlands that could contribute significantly  
61 to carbon emissions during fires (Muller, 2018; Tanneberger et al., 2017). In these ecosystems, the thick litter layer can be  
62 altered by high-temperature peaks reached during fire events, and the soil organic layer can propagate fire by the so-called  
63 smoldering combustion (Watts and Kobziar, 2013). Smoldering is characterized by a slow, flameless combustion that  
64 consumes carbon and releases heat over extensive periods of time. This fire spread mechanism can give rise to overwintering  
65 fires called ‘zombie fires’, which may reactivate during the subsequent fire season, as observed recently in the boreal region  
66 (Irannezhad et al., 2020). Aside from fire safety considerations, these smoldering events could have significant ecological and  
67 atmospheric impacts (Watts and Kobziar, 2013) that have been overlooked in impact assessments and in fire emissions from  
68 European temperate forests (Van Wees et al., 2022; Wiedinmyer et al., 2023), mostly due to the lack of direct evidences and  
69 measurements regarding this process and its extent.

70 During the year 2022 in southwestern France, the region where the largest managed *Pinus pinaster* national forest of 'les  
71 Landes' stands, firefighters consistently raised concerns about lingering soil fires that posed a potential threat for re-ignition  
72 throughout the summer and fall (Ouest-France, 2022). These fires were eventually expected to dissipate with the arrival of  
73 rainfall. However, accurately detecting and monitoring this smoldering combustion using existing Earth Observation Systems  
74 has proven to be challenging. Remote sensing methods are less effective in capturing the fire effects on soils (Johnston et al.,  
75 2018) compared to the canopy (Balde et al., 2023; Fernández-Guisuraga et al., 2022) where changes in surface reflectance can  
76 be observed due to the biomass combustion during fires (Chuvienco et al., 2019) and due to the energy release detected by  
77 thermal sensors (Giglio et al., 2016; Wooster et al., 2021). Unfortunately, the information derived from aboveground  
78 assessments of fire emissions does not correlate well with soil carbon losses (Gerrand et al., 2021) due to the complex  
79 interactions between plant material and soil properties (Varner et al., 2015). Field observations of fire impacts on soils are also  
80 scarce and mainly focused on boreal peatlands (Turetsky et al., 2011a; Mack et al., 2021) or involve extensive time and effort  
81 to assess large-scale areas.

82 To fill this research gap on fire impacts on soil stocks and the subsequent carbon emissions across temperate European forests,  
83 we leveraged the distinctive extreme 2022 fire season in France as a study case. We hypothesized that the atmospheric  
84 signatures of trace gases could serve as a direct indicator of smoldering fires and soil organic matter (SOM) combustion.  
85 Previous investigations of smoldering combustion have shown that this partial combustion results in a high atmospheric  
86 CO/CO<sub>2</sub> ratio (or inversely correlated to the widely used Modified Combustion Efficiency (MCE) index) in the absence of  
87 flaming. Various studies of smoke chemical analysis, including ground-based spectroscopy (Wooster et al., 2011), laboratory  
88 burning experiments (Hu et al., 2019), or drone/aircraft campaigns (Lee et al., 2023) have determined MCE indices ranging  
89 from 0.6 to 0.8 during smoldering combustion. Recent satellite-based studies based on Sentinel-5P (TROPOMI) retrievals  
90 have confirmed these findings by capturing CO plumes from extreme wildfires (Magro et al., 2021). Notably, Hu and Rein  
91 (2022) recently compiled a review on smoldering combustion emission factors, with MCE indices varying from 0.78-0.95 for  
92 flaming in forests to 0.7-0.90 for peatland smoldering combustion. Atmospheric mixing ratios collected by the French  
93 monitoring network, part of the Integrated Carbon Observation System (ICOS, 2023) have been used to document MCE indices  
94 at the regional scale through its wide continental network of atmospheric towers. Seasonal and interannual variations of  
95 greenhouse gas mixing ratios sampled during extreme climate events have been examined in several studies (Heiskanen et al.,  
96 2022; Ramonet et al., 2020). Yet, (Wiggins et al., 2021) remains the only study using the atmospheric tower network to link  
97 low MCE values with smoldering combustion to quantify the CO emissions during the 2015 fire season in Alaska.

98 In our study, we utilized data from the French atmospheric tower network (ICOS - FR, 2023) collected at stations near the  
99 largest fires of 2022 in the temperate forests of les Landes and Brittany, as well as the Mediterranean ecosystems of Provence.  
100 Our objective is twofold : First, to determine if variations in tower-measured MCE could be attributed to fires and to detect  
101 smoldering combustion events; Second, to investigate whether regional variations in MCE are related to specific soil and  
102 vegetation characteristics, fire spread features, or fire intensity indicated by remotely sensed thermal anomalies. These  
103 variables are directly associated with the fire characteristics (Mc Arthur and Cheney, 2015), enabling the detection of

104 smoldering combustion. Finally, we utilized our findings to provide an enhanced bottom-up fire carbon emission framework,  
105 benchmarked with the observed MCE indices, and applied it to the 2022 fire season in France. We also compared our emissions  
106 to GFAS (2023) emissions used by the Copernicus Atmosphere Monitoring Service (CAMS | Copernicus, 2023) as a reference  
107 dataset and publicly delivered in near real-time to stakeholders and society (GFAS | Atmosphere Data Store, 2023).  
108 Desservettaz et al. (2022) warned about substantial mismatches among global datasets when compared to various estimates of  
109 fire-induced CO emissions in Australia incorporating surface in situ data, ground-based total column data, and satellite-based  
110 measurements. Our study contributes to refining the global greenhouse gas budget for national fire risk assessment, considering  
111 carbon stocks as an ecological value in the risk assessment framework developed over the European continent (Chuvieco et  
112 al., 2023).

## 113 **2 Materials and Methods**

### 114 **2.1 Study area**

115 This study focuses on mainland France (41°N-52°N; 5°W-10°E). To facilitate data analysis, we divided the national territory  
116 into four regions based on forest communities and fire occurrence (Fig. 1).

- 117 - Atlantic temperate forest (Sylvoecoregion A11 to A21 according to the National Forest Inventory (NFI) classification)  
118 : This region is primarily characterized by agricultural land, encompassing low vegetation of pasture and cropland.  
119 However, this region comprises dense temperate forests hosting deciduous species (*Quercus. petraea*, *Quercus.*  
120 *robur*, *Fagus. sylvatica*, *Alnus. glutinosa*), with coverage of approximately 11.8%. Historically, this region  
121 experienced low fire incidence owing to its humid oceanic climate, with an annual average of 0.013% ( $\pm 0.006\%$ ) of  
122 the forest area burned (BDIFF, 2023).
- 123 - Atlantic Pine forest (Sylvoecoregion F21 and F22 of the NFI) : This region is almost exclusively covered by extensive  
124 maritime pine plantations (*Pinus pinaster*), cultivated for wood production and covering approximately 76.4% of the  
125 region. Although this region experienced a moderate level of fire activity, with an average annual forest burning area  
126 of 0.062% ( $\pm 0.047\%$ ), large fires were reported in 2022 (Vallet et al., 2023).
- 127 - Mediterranean forest (Sylvoecoregion J10 to K13 of the NFI): This region is characterized by low, dense forests  
128 (covering 39.8% of the region) dominated by species typical of the Mediterranean climate (*Quercus. ilex*, *Quercus.*  
129 *pubescens*, *Quercus. suber*, *Pinus. halepensis*). This region experiences a high frequency of fires, with approximately  
130 0.25% ( $\pm 0.21\%$ ) of the forest area burned each year.
- 131 - Other temperate forests encompass the remaining forested land of France. This region comprises diverse temperate  
132 forest communities covering 28.3% of the area, dominated by deciduous or coniferous species and exhibiting varying  
133 levels of management intensity. Historically, this region experienced minimal fire occurrence, with an average annual  
134 forest burning area of 0.016% ( $\pm 0.002\%$ )

## 135 **2.2 Fire data**

### 136 **2.2.1 Fine resolution fire polygons**

137 For the fire season 2022, we delimited fire polygons using the semi-automated Burned Area Mapping Tools (BAMTs)  
138 (Bastarrika et al., 2014; Roteta et al., 2021). This method was exclusively applied to fires exceeding 30ha and over ignitions  
139 captured by the Visible Infrared Imaging Radiometer Suite (VIIRS, onboard the Suomi and NOAA-20 satellites) within  
140 wildlands (Schroeder et al., 2014). VIIRS data experience a temporal resolution of roughly 6 hours and detects land surface  
141 thermal anomalies (1000K) at 375m resolution so that small and fast spreading fires can be missed. Yet, this information has  
142 been shown to be reliable for fires above 10ha in Mediterranean areas (Majdalani et al. 2022). BAMTS uses on atmospherically  
143 corrected and orthorectified images from the L2A product of ESA’s Sentinel-2 mission of 2022, to derive three key spectral  
144 indices : Normalized Differential Vegetation Index (NDVI) (Rouse et al., 1974), Normalized Burn Ratio (NBR) (Key and  
145 Benson, 1999), and NBR2 (García and Caselles, 1991). We used the VIIRS-derived fire dates to set pre- and post-burn  
146 timeframe to capture the difference in these three indices between the two periods, and represented in an RGB color scale.  
147 Specifically, the pre-fire period extended from the onset of the year (January 1st) up to the earliest date of hotspot clusters  
148 identified by VIIRS. The post-fire period encompassed several weeks after the fire ignition and ensured a sufficient number  
149 of cloud-free satellite images. Through a visual examination of the RGB spectrum, we manually defined two sample training  
150 region, one being within the high signal differences and considered as burned, the other within the low signal difference and  
151 considered as unburned.. A random forest classifier (Belgiu and Drăguț, 2016) then classifies each pixel of the study area as  
152 burned or unburned according to its spectral indices similarity to the one or the other training region. A quality assessment of  
153 the automatically processed classification was performed through visual inspection (cf Vallet et al. 2023) and training regions  
154 were fine-tuned if obvious misclassifications were detected. This key step, unavailable in current automated methods, ensures  
155 the international standards advocated by the CEOS Working Group on Calibration and Validation of remote sensing datasets  
156 (Franquesa et al., 2020). Focusing on fires exceeding 30 ha and confined to the fire season (June to September), we identified  
157 a total of 70 fire polygons in the year 2022. These fire polygons were primarily located in forested and shrubland areas. Among  
158 these fire polygons, we studied only three of them located in the proximity of atmospheric towers for in-depth analysis of  
159 emissions, further referred to as “main fires” (description in table 3). These three fires were the largest occurring in each region  
160 in the fire season 2022.

### 161 **2.2.2 Fire intensity and fire spread**

162 To enhance the precision of our analysis regarding fire behavior during propagation, we incorporated supplementary data,  
163 specifically surface thermal anomaly information for active fire detection. This data was gathered from MODIS (Moderate  
164 Resolution Imaging Spectroradiometer) instruments on Terra and Aqua satellites (MCD14ML) (Giglio, Louis, 2000),  
165 featuring a spatial resolution of 1 km. Additionally, we harnessed VIIRS (Visible Infrared Imaging Radiometer Suite) data  
166 from the SNPP (Suomi National Polar-orbiting Partnership) and NOAA-20 (National Oceanic and Atmospheric

Administration) sources, offering a finer spatial resolution of 375 m (Schroeder et al., 2014). The acquisition of these datasets was facilitated through the utilization of the Fire Information for Resource Management System (NASA-FIRMS, 2023). Subsequently, we executed a spatial filtration process to exclude all thermal anomalies occurring outside the confines of our designated fire patches.

The thermal anomalies derived from these data sets were instrumental in our analysis, primarily regarding assessing the intensity of fires during their propagation. We gauged this by examining the Fire Radiative Power (FRP) values, a recognized indicator of combustion intensity (Wooster et al., 2005). Furthermore, to gain insights into the direction and daily rate of fire spread, we leveraged the temporally dated (3 to 9-hour intervals) spatial locations of fire hotspots. Employing an ordinary kriging method, a geostatistical interpolation technique available through the gstat R package (Gräler et al., 2016), we used the timing (expressed in decimal days) as the target variable for interpolation, similar to previous studies (Parks, 2014; Veraverbeke et al., 2014; Scaduto et al., 2020). For each main fire, we manually fine-tuned a Gaussian or Spherical function to derive the best-fitted variogram. Finally, we computed the hotspot density (number per hectare) within each fire polygon over the entire fire duration. This approach allows us to capture protracted soil and peatland fires that exhibit either a heightened hotspot density or an extended burning period (Usman et al., 2015).

### 2.3 Atmospheric CO/CO<sub>2</sub> mixing ratio analysis

In this study, we collected hourly measurements of CO and CO<sub>2</sub> mixing ratios derived from a subset of instrumented towers part of the French monitoring network (SIFA, 2023), a network established for monitoring atmospheric greenhouse gas variations in the atmosphere. These measurements were conducted with high-precision cavity ring-down spectroscopy (CRDS), with up to three sampling levels (Conil et al., 2019; Lelandais et al., 2022; Lopez et al., 2015; Schmidt et al., 2014). The selected stations, outlined in Table 1, include distant stations and nearby stations located within 20 km of the 2022 large fires that occurred in the Atlantic temperate forests (Brittany), Atlantic pine forests (Landes), and Mediterranean forests. Data collection for this study spanned from June 15th to September 1st, 2022. In the context of the Atlantic pine forest that started on July 12th, the dominant winds were from the northeast, propelling the plume seaward. Notably, a shift in wind direction occurred on July 14<sup>th</sup>-15<sup>th</sup>, with the wind veering to the north-northwest. This shift contributed to the highest CO peaks observed at the Biscarrosse (BIS) station. Subsequently, on the 19<sup>th</sup>, the wind shifted westward, transporting the plume inland and leading to elevated CO concentrations at distant stations. Similarly, in the Atlantic temperate forest (Brittany), predominant winds came from the northeast, steering the plume away from the Roc'h Trédudon (ROC) station toward the ocean. Changes in the wind direction led to intermittent CO signals at the ROC station. The only instance when the plume was transported inland occurred on July 19<sup>th</sup>.

To determine the locations of the sources corresponding to the identified CO mixing ratio anomalies observed at the atmospheric towers, we computed back-trajectories representing the different air masses sampled at the tower locations. This step was accomplished using the Hybrid Single Particle Lagrangian Integrated Trajectory (Hysplit) model (Stein et al., 2015). In a backward-in-time configuration, particles were released from the receptor site and monitored over 7-day intervals. The

200 result is a footprint matrix representing the influence of the area around the receptor on the measurements. The model spatial  
201 resolution used is  $0.05 \times 0.05$  deg. The Global Forecast System (GFS) meteorological model (National Centers For  
202 Environmental Prediction/National Weather Service/NOAA/U.S. Department Of Commerce, 2015) provided the atmospheric  
203 conditions (wind and turbulence) to drive these particles from the receptors to the sources in the Hysplit simulations. The GFS  
204 outputs, featuring a horizontal resolution of  $0.25^\circ \times 0.25^\circ$  and 3-hourly time intervals, served as the meteorological inputs. We  
205 also conducted Hysplit simulations in a forward-in-time configuration releasing particles (600 per hour) from the fire locations,  
206 over the fire duration from the exact burned area. . In this configuration, we simulated the transport of the plume from the fires  
207 to the ICOS stations. By tracking the arrival times of the fire-emitted-particles within an influence region surrounding each  
208 atmospheric tower, we successfully attributed a fire source to each anomaly. These influence areas featured varying radii to  
209 account for transport uncertainties, considering that the minimum distance between the towers and the nearest fires ranged  
210 from 7 to 650 km. For towers in proximity to active fires (within 20 km), the influence radius was set at 4.5 km, corresponding  
211 to a single hysplit-grid cell. For more distant towers, the influence radius was extended to 25 km to account for errors associated  
212 with long-distance transport.

213 To quantify the excess in CO and CO<sub>2</sub> mixing ratios originating from the fires, we needed to determine the background  
214 concentration levels that would have been observed in the absence of fires. Due to the extensive duration of some observed  
215 fire events (>10 hours), a simple interpolation method could not be used without impacting our enhancements with variations  
216 in the background air (diurnal cycle, sea breeze periods...). To determine the background flow more accurately, we trained a  
217 Random Forest (RF) regression model for each gas at each station. The RF model is a non-parametric statistical method based  
218 on averaging over ensembles of multiple regression trees (Breiman, 2001). In our approach, we randomly divided the  
219 atmospheric observations into three categories: 1) the studied data, 2) the training data, and 3) the testing data. Initially, we  
220 isolated the data that were indicative of forest fires contributions to the observations. These periods were characterized by  
221 elevated CO mixing ratios and were automatically identified as outliers by the Tukey's fence approach (Tukey, 1977).  
222 Subsequent manual quality checks ensured that the flagged data coincided with the active forest fire periods. The remaining  
223 data were then divided into training (70% or approximately 1000 data points) and testing (30% or around 400 data points) sets  
224 for each station separately individually. In addition to the mixing ratios, meteorological and calendar data were included as  
225 input variables for the RF models. The meteorological data encompassed parameters such as 10 m wind speed and direction  
226 (m.s-1), 2 m Temperature (°C), and Boundary Layer Height (BLH) (m). The meteorological data encompassed the following  
227 parameters: 10 m wind speed and direction (m.s-1), 2 m Temperature (°C), and Boundary Layer Height (BLH) (m). These  
228 meteorological parameters were extracted from the ERA5 hourly reanalysis dataset (Hersbach et al., 2020). Time-derived  
229 variables included the hour of the day, day of the week, day of the month, and month of the year. For the RF model, the number  
230 of regression trees was set at 100.

231 The RF model performance was assessed using the testing data, with evaluation metrics including the coefficient of  
232 determination (R<sup>2</sup>) and the root-mean-square error (RMSE). The model's performance scores exhibited variability across sites.

233 On average, we achieved a correlation of 0.77 and 0.97, along with an RMSE of 7.66 ppb and 1.12 ppm for CO and CO<sub>2</sub>,  
234 respectively (Table 1).

235 The excess mixing ratios of CO and CO<sub>2</sub> attributable to the fires, denoted as  $\Delta[\text{CO}]$  and  $\Delta[\text{CO}_2]$ , were calculated as the  
236 difference between the observed mixing ratios and the simulated background mixing ratios generated by our RF model.  
237 Subsequently, we computed the modified combustion efficiency (MCE), with values indicating higher levels during flaming  
238 fires combustion and lower levels during smoldering fires, according to Equation (1) (Hao and Ward, 1993; Yokelson et al.,  
239 1996):

$$240 \quad MCE = \frac{\Delta[\text{CO}_2]}{\Delta[\text{CO}_2] + \Delta[\text{CO}]} \quad 241 \quad (1)$$

## 242 **2.4 Above- and below- ground dry matter stock**

243 To further comprehend the origin of the MCE observed at the monitoring towers, we sought to estimate the carbon pools  
244 affected by the fires, possibly contributing to the emissions of CO and CO<sub>2</sub>. Given that our analytical framework relies on  
245 emission factors (EF) expressed in grams of gas emitted per kilogram of dry matter (DM) consumed, we expressed these pools  
246 in units of tons of dry matter. The entirety of the ecosystem dry matter stock is partitioned into two distinct types : the  
247 aboveground stock (AGS) and the belowground stock (BGS). Each of these stock types encompasses multiple pools. The AGS  
248 comprises the stem, branch, leaf, shrub, grass, and litter pools, while the BGS includes Soil Organic matter (SOM), peat, and  
249 lignite pools.

### 250 **2.4.1 Forest stem and branch pool**

251 Within the AGS affected by fires, the stem and branch pools are prominent components. These pools align with the woody  
252 AGB-L (Above-ground biomass loss) method introduced by Vallet et al. (2023). This method is based on two high-resolution  
253 data sources: first, a 10-m resolution mapping of vegetation height obtained from GEDI, Sentinel 1, and 2 satellite images  
254 from 2020 (Schwartz et al., 2023); second, data indicative of forest communities and individual descriptors, sourced from  
255 French National Forest Inventory (NFI) since 2005 (IFN, 2023a). Data supplied by the NFI within a 5-km radius of fire was  
256 used to delineate individual and population allometric relationships.

257 Based on the remotely-sensed data on vegetation height, we estimated the biomass of a model tree within each burned pixel.  
258 Subsequently, for each pixel, we determined a tree density based on the biomass of the model tree and the density-dependency  
259 relationship derived from NFI data. After applying the AGB-L method to each 10-m burnt pixel, we segregated the above-  
260 ground forest biomass into stem pool and branch pools. Deciduous branches accounted for 39% of the above-ground biomass,  
261 while coniferous branches contributed 25% (Loustau, 2010).



#### 262 **2.4.2 Shrub, grass, and litter pools**

263 To account for AGS affected on non-forest pixels (where the height is less than 3m), we applied a fixed biomass (dry weight)  
264 density value of 10tDM.ha<sup>-1</sup> for shrubland vegetation and 4tDM.ha<sup>-1</sup> for herbaceous vegetation (Vallet et al., 2023). These  
265 values are in agreement with the stocks included in the FINN carbon emission model (Wiedinmyer et al., 2023). Pixels were  
266 classified as containing shrubland vegetation based on the presence of sclerophyllous vegetation in the CORINE LAND  
267 COVER database (CORINE Land Cover 2018, 2023), along with a recorded vegetation height below 3m. Pixels not classified  
268 as forest or shrubland were considered as grassland.

269 The litter pool was also incorporated into the AGS. It was derived from the GFED5 dataset, available at a resolution of 500-m  
270 by (Van Wees et al., 2022). We resampled this fine litter data to a 10-m resolution using the nearest-neighbor method.

#### 271 **2.4.3 Forest and shrubland leaf pool**

272 The leaf pool, representing the fraction of vegetation most completely consumed during combustion, was quantified based on  
273 a combination of satellite data and in situ measurements of leaf traits. Leaf area index (LAI) data at a resolution of 300m were  
274 derived from the Sentinel-3 LAI product provided by the Copernicus service (Verger et al., 2014). These data were compiled  
275 over the summer period of 2022 (June to September), and the average of the non-zero values for each pixel was extracted.  
276 Specific Leaf Area (SLA, in m<sup>2</sup>.kgDM<sup>-1</sup>) was obtained at a resolution of 500 m from the TRY database (Moreno-Martínez et  
277 al., 2018). To calculate leaf mass, we initially conducted a nearest-neighbor resampling of LAI and SLA maps at 10 m  
278 resolution. Subsequently, the leaf pool density (kgDM.m<sup>-2</sup>) was determined by dividing the LAI values (m<sup>2</sup>.m<sup>-2</sup>) by the SLA  
279 values (m<sup>2</sup>.kgDM<sup>-1</sup>) for each pixel. Only pixels categorized as forest or shrubland (height >3m) were included in this leaf pool  
280 dataset.

281 Consequently, the AGS is then composed of 6 pools : stem, branch, leaf, shrub, grass, and litter.

#### 282 **2.4.4 Soil Organic Matter (SOM) pool**

283 The Soil Organic Matter (SOM) is encompassed within the BGS. Data for this pool was sourced from the European Soil Data  
284 Centre (ESDAC) (yigini & panagos, 2016), offering carbon density values (tC.ha<sup>-1</sup>) for the top 20 cm of soil at a resolution  
285 of 1000 m. To determine the pool of soil organic matter within each burned pixel, we converted these carbon values into  
286 organic matter, assuming a carbon content of 0.5 (Pribyl, 2010). This data was then resampled at 10-m resolution using the  
287 nearest-neighbor approach.

#### 288 **2.4.5 Other belowground pools : peatland and lignite**

289 To investigate the sources of smoldering combustion and pyrolysis, we considered two additional pools within the BGS.  
290 Marshland areas, particularly peatland, can potentially contain huge amounts of organic matter, which is often assumed as  
291 insignificant in temperate forest fire emissions. During the summer, waterlogged areas can become vulnerable to fire as they

292 dry out. To account for peatland areas, we relied on the CORINE LAND COVER (CLC) database (CORINE Land Cover  
 293 2018, 2023). We established a fixed characterization of the peatland, assuming a depth of 2 m and a mass density of 145  
 294 kgDM.m<sup>-3</sup>, as measured in France (Pilloix, 2019). We then calculated the pool mass for any point within the CLC polygon by  
 295 multiplying the pixel area (~100 m<sup>2</sup>) by the depth and biomass density.

296 Lignite is a distinctive pool within the BGS found in ‘Les Landes’, arising from a slow decomposition process. Historically,  
 297 lignite has been utilized as an energy source in Les Landes, near the city of Hostens, for its high concentration of carbon.  
 298 Firefighters in this area reported high soil temperatures near the ancient mines. The lignite layer is near the surface and located  
 299 beneath the organic soil. The location of the lignite area was provided by the APPHIM association (apphim.fr - Les gisements  
 300 de charbon et lignite, 2023) around the Hostens village. The lignite mine typically has a depth ranging from 2 to 5m, extending  
 301 to 10-15 m. For our analysis, we assumed a fixed depth of 2 m (Le lignite d’Hostens, 2023). The bulk density of brown coal  
 302 is generally around 700kgDM.m<sup>-3</sup> (Coal - Carbon, Organic Matter, Sedimentary Rock | Britannica, 2023). Accordingly, the  
 303 density of the lignite pool was set at 1400kgDM.m<sup>-2</sup> of burned surface. This particular pool of carbon has been affected by  
 304 two large fires during the 2022 fire season.

305 Thus, the BGS encompasses three pools: Soil Organic Matter (SOM), peat, and lignite.

## 306 2.5 Carbon emissions

307 Utilizing information from fire polygons (Fig. 2, ‘Database’) and estimation of AGS and BGS pools (Fig. 2, ‘Stock’), we  
 308 estimated CO<sub>2</sub> and CO emissions arising from two combustion phases, namely, flaming (F) and smoldering (S). This  
 309 quantification was computed for each of the AGS (stem, branch, leaf, shrub, grass, litter) and BGS (SOM, peat, lignite) pools.  
 310 Emission assessment was facilitated by accounting for two crucial factors : the combustion completeness (CC), denoting the  
 311 proportion of the pool altered by combustion, and emission factors (EF, in g.kg<sup>-1</sup>DM) for CO<sub>2</sub> and CO. For each individual  
 312 pixel within the fire patch ( $p$ ), each specific pool ( $P$ ) (Table 2) and each gas ( $x$ ), we calculated emission ( $E$ ) using the following  
 313 formula (2) :

$$314 \quad E_{Px} = M_p * CC_p * (SF_p * EF_{PxS} + (1 - SF_p) * EF_{PxF}) \quad 315 \quad (2)$$

316  $E_{Px}$  : Emission of gas  $x$  from pool  $P$  (g)

317  $M_p$ : dry Mass of pool  $P$  (kgDM)

318  $CC_p$  : Combustion completeness of pool  $P$  (percentage of available pool)

319  $SF_p$  : Smoldering fraction of pool  $P$  (percentage of combusted pool in smoldering phase)

320  $EF_{PxS}$  and  $EF_{PxF}$  : Emission factors for pool  $P$  into gas  $x$ , during smoldering ( $s$ ) and flaming ( $f$ ) phase. (g.kg<sup>-1</sup>DM)

321

322 To calculate the emissions of gas  $x$  (Fig. 2, ‘Emission’) from all pools ( $n$  pools  $P$ ) within each burned pixel ( $p$ ), we utilized the  
 323 following equation (3) :

$$324 \quad E_{px} = \sum_{p=1}^n E_{Px} \quad 325 \quad (3)$$

326

327 Consequently, we were able to obtain an aggregated emission value for gas  $x$  encompassing the entire fire ( $A$ ) comprising  $m$   
 328 individual pixels  $p$ , as specified in equation (4) :

$$329 \quad E_{Ax} = \sum_{p=1}^m E_{px} \quad 330 \quad (4)$$

331

332 Table 2 provides a comprehensive summary of CC, EF, and SF for each pool, drawing from a bibliographical review of  
333 available data from global fire emission models, such as GFED (Van Wees et al., 2022) and FINN (Wiedinmyer et al., 2023),  
334 along with empirical field measurements conducted in temperate forests. Notably, in the absence of specific data synthesis for  
335 Europe, the fraction of smoldering combustion for each pool was inferred from data collected in American temperate forests  
336 (Prichard et al., 2020). We provide a range of values for combustion completeness ( $CC_{\min}$  and  $CC_{\max}$ ). The estimated values  
337 for combustion matter (M), emission (E) and MCE correspond to the average between the minimum and maximum estimates.  
338 The uncertainty ranges correspond to the deviation between this mean value and the limit value (min or max value having the  
339 same deviation from the mean).

340 To provide comparable information between our fire-level emissions and the hourly MCEs derived from measurement  
341 obtained by the atmospheric towers, we set up three distinctive stages in the fire propagation:

- 342 1) The spreading stage (SS), where the AGS constitutes the entire combustion. 50% of AGS is affected during this phase.
- 343 2) The mixed stage (MS), characterized by ongoing aboveground flaming at the fire front while smoldering combustion  
344 consumes the wood residual and BGS over the previously burned area. This stage involves 50 % of AGS and 25% of BGS.
- 345 3) The post-spreading stage (PSS), devoid of flaming but marked by continuing smoldering in the soil and wood residuals,  
346 representing the totality of emissions. 75 % of BGS is impacted during the post-spreading stage.

347 The splitting of the BGS smoldering at 75% during the post spreading stage and 25% during the mixed stage relies on the  
348 flaming duration of 10 days for the BIS fire and with an extended 15 days (to be conservative) after the spreading. The mixed  
349 stage lasted 5 days, representing 25% of the smoldering period lasting these 5 days plus the 15 days after the spreading (20  
350 days of smoldering duration). This is a conservative value as smoldering lasted for longer but with way less intensity. We also  
351 tested for accurate MCEs during this mixed stage (cf flowchart figure A1) to keep this fraction.

352 These three stages have been applied to the three main fires and calibrating the combustion completeness of each pool. More  
353 precisely, we tested different sets of CC values until the model MCEs and the tower-measured MCEs corresponded. Once the  
354 refined CC were defined, we applied this fire model to all the fire polygons obtained in 2022. Belowground combustion (i.e.  
355 BGS combustion) was only applied to fires corresponding to selected criteria for smoldering (Fig. A1).

356 For comparison, we utilized the Global Fire Assimilation System (GFAS, 2023) dataset for fire emissions (Kaiser et al., 2012).  
357 This dataset is the only one to offer near-real-time coverage extending up to 2022, generating daily emissions based on MODIS  
358 MCD thermal ‘hotspots’ anomalies and biome-specific combustion rate (in kgDM.MJ-1). GFAS delivers information at a  
359 0.1° resolution, covering burnt dry matter, fire emissions, and injection height on a daily basis since 2003, with near-real-time  
360 updates. We accessed GFAS data for CO<sub>2</sub> and CO emissions for the period spanning from June to September 2022, considering  
361 the entire dataset within this timeframe for our analysis.

363 **3.1 Attribution of the MCE to the various fires**

364 In order to disentangle the inherent CO and CO<sub>2</sub> background mixing ratios at the atmospheric tower stemming from prevailing  
365 atmospheric conditions, and the emissions originating from actual fires, we initiated a rigorous assessment of our Hysplit  
366 atmospheric transport simulations and their alignment with the detected tower overpasses. Fire plume shapes and directions  
367 can be qualitatively evaluated when smoke is visible in visible satellite imagery. Figure 3 visually demonstrates the  
368 correspondence between observed plume positions, detected by MODIS, and the modeled plume positions, particularly in the  
369 case of the Landes fires. Notably, both the observed and modeled plumes exhibited a correct overlap, reinforcing the precision  
370 of our modeled wind direction changes as corroborated by the analysis of the comprehensive suite of satellite snapshots  
371 available throughout the study period.

372 It is worth mentioning that, during the same study period, TROPOMI data showed the arrival of an air mass with elevated CO  
373 concentrations from Spain, where forest fires were occurring at the same time (not shown here). However, we did not account  
374 for those fires in the current study, since the analysis of the HYSPLIT Lagrangian model results indicated a minimal impact  
375 from these fires on the time series monitored at the French towers, as evidenced by both forward and backward-in-time  
376 simulations. Specifically, the results of the Lagrangian model indicated that the stations CRA and PUY were largely unaffected  
377 by these fires. The analysis also showed that many signals from OHP were mixed with anthropogenic sources and had to be  
378 discarded. The plumes from both the Landiras and Mont d'Arrée fires were mixed before reaching the inland stations of MDH,  
379 OPE, SAC, TRN. Consequently, we opted to exclude these towers from the MCE analysis, reserving their data solely for the  
380 evaluation of the RF background estimates. At each of the three remaining sites, namely BIS, OHP, and ROC, only the  
381 influence of the adjacent fire was observed: Landiras1 for BIS, La Montagne for OHP, and Monts d'Arrée for ROC.

382 The analysis of the MCE index during the days when the simulated particles reached the atmospheric tower locations shows  
383 that the MCE signatures associated with the fires exhibit regional variations. In particular, the fire near BIS displayed a median  
384 MCE of  $0.83 \pm 0.03$ , the lowest mean value among the three sites (Fig. 4). The BIS-values correspond to the MCE values that  
385 are observed most often under smoldering combustion phases and high-temperature pyrolysis phases. In contrast, the OHP fire  
386 predominantly featured MCEs exceeding 0.95, marked by low variations, with a minimum value of 0.93, primarily observed  
387 during flaming combustion. The ROC site collected intermediate values, with a median MCE of 0.94, close to the  
388 Mediterranean MCE observed at OHP. However, ROC exhibited minimum values that reached 0.82, far lower than the values  
389 observed at OHP. This variation suggests the occurrence of smoldering combustion phases throughout the fire propagation.  
390 Daily MCE variations (Fig. 4) emphasized a decreasing trend for the BIS fire, indicating an increase in smoldering combustion  
391 over time, supporting the hypothesis of a prolonged soil combustion following the cease of spreading stage. Conversely, this  
392 temporal pattern was less discernible for the fast-spreading ROC fire.

393 Furthermore, we looked into the 1-minute averaged concentrations to investigate rapid changes in combustion, fire  
394 propagation, atmospheric transport, and the implications of different averaging periods on our analytical results. We found

395 that the MCE values derived from both the 1-minute and 1-hour averaged mixing ratios are consistent, as shown in Fig. 4.  
396 While there is a broader dispersion in the case of the 1-minute sampled mixing ratios, the fire MCE signal remained consistent  
397 across all stations. Notably, when accounting for the uncertainty in the RF estimates, the MCE varied by 2% when propagating  
398 the mean error from the RF model for CO and CO<sub>2</sub>. This variation had no discernible impact on the overall findings of this  
399 study, ensuring the consistent differentiation of the combustion types attributed to the main fires.

### 400 **3.2 Exposure and stock affected**

401 To disentangle the fire behaviors associated with the observed MCE indices measured at the towers located within the Atlantic  
402 temperate forest (ROC), Atlantic pine forest (BIS), and Mediterranean forest (OHP), we performed a comprehensive  
403 characterization of the affected AGS and BGS by these main fires.

404 The ROC fire, encompassing a total area of 1,726 hectares, primarily impacted low vegetation, with grassland covering 63.3%  
405 of the burned area (Table 3 and Fig. A2). The fire's influence on forest area was comparatively limited, spanning only 129 ha,  
406 characterized by a low biomass density of approximately 46tDM.ha<sup>-1</sup>. A distinguishing feature of this fire is the substantial  
407 presence of peatland, occupying 449ha (26% of the burned area). Remarkably, the aggregated stock, combining AGS and  
408 BGS, is largely dominated by the peatland pool, accounting for 86.9% of the total stock. We note here that this pool is  
409 recognized for its propensity to combust predominantly through smoldering.

410 The BIS fires extended over a considerably larger area of 12,140 hectares and predominantly affected forested areas (71% of  
411 the burned area) characterized by high biomass density ranging from 20 tDM.ha<sup>-1</sup> to 150 tDM.ha<sup>-1</sup> (see Fig. A2 'Vegetation').  
412 Moreover, the SOM in this region falls within the highest range of the country, varying between 210 and 250 tDM.ha<sup>-1</sup>, a  
413 noticeably larger amount compared to the temperate Atlantic (100-220 tDM.ha<sup>-1</sup>) and Mediterranean (70-120 tDM.ha<sup>-1</sup>)  
414 regions (Fig A2, 'SOM'). Additionally, this fire also altered 61 hectares of peatland. An unusual feature of this area is the  
415 presence of a lignite layer situated near the surface, spanning 1,909 hectares within the burned area (15.7%). Remarkably, the  
416 lignite pool constitutes 88.0% of the total dry matter stock (AGS and BGS), followed by the SOM pool (9.4%). These two  
417 significant pools, lignite (combusted at high temperature during the pyrolysis phase) and SOM (mostly smoldering), both  
418 contribute to a substantial stock of carbon that is potentially affected, resulting in low MCEs.

419 Finally, the OHP fire in the Mediterranean region primarily affected forests (76.1%), along with low vegetation zones like  
420 garrigue (shrubland = 15.3% and grassland = 8.6%). Forest biomass in this area, however, falls within the low range of biomass  
421 density observed in the country, with a median of 60.4 tDM.ha<sup>-1</sup>, and the soil contains relatively low amounts of organic matter  
422 (95.2 tDM.ha<sup>-1</sup>). Conversely, the aggregated stock (BGS and AGS) density, amounting to 147 tDM.ha<sup>-1</sup>, stands in stark contrast  
423 to the fires in Atlantic pine forests (2,502 tDM.ha<sup>-1</sup>) or Atlantic temperate forests (867 tDM.ha<sup>-1</sup>).

424 As a first step toward identifying potential factors contributing to the lower MCEs in the BIS and ROC fires, we illustrate here  
425 that the fires with the lowest minimal MCEs (ROC, BIS) occurred in areas marked by the highest belowground organic density.  
426 Smoldering features shown by these fires have been either favored by carbon-enriched zones, such as peat bogs or lignite, or,  
427 as seen in the Landes region, featured a high SOM density.

### 428 **3.3 Fire characterization**

429 To discern whether specific fire characteristics could effectively distinguish fires affecting BGS, we conducted an assessment  
430 based on key parameters, such as the extent, duration, rate of spread, and intensity with 6-hourly Fire Radiative Power (FRP).  
431 Among the study sites, the maximum FRP was observed during the OHP fire, reaching 359 MW, followed by BIS with 299  
432 MW and ROC with 150 MW (Fig. A3). ROC and OHP fires exhibited a relatively short duration of high FRPs, extending up  
433 to three days, in contrast with the BIS fire, where the period of high FRP persisted for eight days. However, when examining  
434 low-intensity FRPs, a discerning pattern emerged. The OHP fire showed no remaining burning activity beyond the initial three  
435 days of high-intensity combustion. In contrast, the ROC and BIS fires exhibited a protracted signal, spanning up to 25 days  
436 after ignition for ROC and 32 days after ignition for BIS (Fig. A3). This information appears pivotal for distinguishing fires  
437 characterized by low MCEs.

438 Furthermore, an evaluation of the fire rate of spread (ROS) within the burned area (Fig. 5) revealed distinct patterns. The BIS  
439 fire displayed a notably high hotspot density of  $0.27 \text{ hotspot.ha}^{-1}$ , combined with a relatively slow ROS at  $0.147 \text{ km.h}^{-1}$ . In  
440 contrast, the ROC fire expanded rapidly (median ROS =  $1.77 \text{ km.h}^{-1}$ ), along with a markedly lower hotspot density of  $0.055$   
441  $\text{hotspot.ha}^{-1}$ . In particular, this fire spread relatively rapidly over grasslands, even when compared to the OHP fire, which  
442 occurred over shrublands and Mediterranean vegetation ( $0.66 \text{ km.h}^{-1}$  with  $0.05 \text{ hotspots.ha}^{-1}$ ).

443 Based on the characteristics related to propagation and combustion, we conclude that fires prone to experiencing smoldering  
444 combustion, such as BIS and ROC fires, exhibit a prolonged duration of hotspots after ignition, which is not observed for the  
445 OHP fire. This index could be used for ‘a posteriori’ fire emission quantification, yet hardly usable for near-real time  
446 assessment The median ROS or maximum fire intensity does not appear to be discriminating factors between fires impacting  
447 aboveground and belowground stocks.

### 448 **3.4 Bottom-up approach on carbon emissions**

449 Leveraging our estimation of both AGS and BGS in each of BIS, ROC, and OHP fires, we undertook a bottom-up assessment  
450 of MCEs. This assessment compared our MCE estimates to the ranges of combustion and emission factors values estimated  
451 by previous studies. In our initial approach, we conducted the basic calculations akin to those employed in global fire emissions  
452 models for temperate forests, exemplified by GFAS and FINN. This approach exclusively accounted for AGS and focused  
453 only on flaming combustion (Table 4, ‘AGS only’). The resulting MCEs ranged from 0.955 to 0.961 for all the fires, with no  
454 significant distinctions between them. While these values closely mirrored the median MCEs observed at the OHP tower with  
455 low variability, they notably diverged from the range of MCEs captured at the ROC and BIS stations.

456 In our subsequent approach, we incorporated belowground combustion effects for ROC and BIS. We divided the combustion  
457 process into three distinct stages (spreading stage, mixed stage and post-spreading stage). For the ROC fire, the calculated  
458 MCE values for the spreading stage were  $0.961 (\pm 0.001)$ , aligning with the median value obtained from the hourly mixing  
459 ratios measured at the ROC tower. Subsequently, for the mixed stage, MCE values of  $0.828 (\pm 0.015)$  were derived,

460 corresponding to the lower range of 1-h mixing ratios. Finally, for the post-spreading stage, MCE values of  $0.796 (\pm 0.001)$   
461 were obtained, similar to the minimum values observed within the distribution of the 1-min mixing ratio.  
462 Considering the BIS fire, the results for the spreading stage exhibited MCE values of  $0.956 (\pm 0.004)$ , values corresponding to  
463 the upper bounds of observations collected at the BIS tower. Subsequently, for the mixed stage, MCE values of  $0.821 (\pm 0.015)$   
464 were calculated, representing the respective median values from the 1-hour mixing ratio and the 1-min MCE. Finally, for the  
465 post-spreading stage, an MCE of  $0.729 (\pm 0.011)$  was derived, indicating a significant occurrence of smoldering combustion  
466 rate, and closely mirroring the minimal values obtained for the 1-hour MCE measured at this tower.  
467 This refined bottom-up approach, including soil smoldering combustion, successfully captured the spectrum of MCEs observed  
468 at the ICOS atmospheric towers. These findings, which could not be obtained from aboveground combustion alone, underscore  
469 the significance of accounting for belowground combustion when addressing the carbon emission budget.

### 470 **3.5 Fire emissions assessment in 2022 for France**

471 Drawing from our MCE-calibrated carbon emission framework of AGS-BGS combustion, we applied our refined carbon  
472 emission framework to the 70 fires exceeding 30 ha, which were accurately mapped across France. Smoldering combustion  
473 was exclusively attributed to fires affecting vegetation types similar to the BIS and ROC fires, namely those encompassing at  
474 least one of the following criteria: needle leaves and high SOM values; prolonged hotspot signal after the end of fire spread;  
475 peatlands, and/or lignite (Fig. A1).

476 The year 2022 witnessed a significant impact of fires in the Atlantic pine forest region, with a total burned area of 26,850 ha  
477 (Fig. 6), constituting 64.5% of the overall burned area. Ranked second, the Mediterranean region experienced several fires  
478 over 7,600 ha, accounting for 18.2% of the total burned area. Fires mainly altered forest areas in the Atlantic pine region  
479 (76.5%) and other forest (75.6%) regions. Regarding the Mediterranean region, fires influenced both forest (45.4%) and low  
480 vegetation, including shrubland (11.0%) and grassland (43.6%). In the Atlantic temperate forest, grasslands were the most  
481 affected, encompassing 59.2% of the burned area.

482 In our estimation, out of the total 44.68 MtDM of stock impacted by fires in 2022 and potentially lost, only  $4.526 (\pm 2.138)$   
483 MtDM was actually combusted and directly released into the atmosphere (Table A1). The Atlantic pine forest region  
484 contributed to the majority of this combusted matter due to its particularly high burned area and its substantial densities of  
485 AGS and BGS. More precisely, its AGS accounts for  $28.2\% (\pm 1.9)$ , and its BGS for  $54.1\% (\pm 2.6)$ . Moreover, the Atlantic  
486 temperate forest contributed significantly to the total stock combusted, when considering BGS, primarily due to the presence  
487 of peatlands, accounting for  $5.2\% \pm 0.3$ . In contrast, AGS combustion in the other three regions outside the Atlantic pine forest  
488 was responsible for only  $12.5\% (\pm 0.9)$  of the total stock loss.

489 Our estimates indicate that the fires of 2022 directly emitted  $6.154 (\pm 2.650)$  Mt of  $\text{CO}_2$ , with AGS and BGS contributing  
490 nearly equally to these  $\text{CO}_2$  emissions. Specifically, all AGS were found responsible for  $49.5 (\pm 2.9)\%$  of the annual  $\text{CO}_2$   
491 emissions, with the remainder attributed to BGS, particularly SOM and lignite from the Atlantic pine forest region ( $46.4 \pm$   
492  $2.7\%$ ). In comparison, the GFAS framework estimated that summer fires were accountable for 3.86 Mt $\text{CO}_2$  emissions, when

493 not considering mid-latitude extra-tropical potential BGS combustion and small peatland distribution, a value that corresponds  
494 to the lower bound of our estimations when considering our uncertainties on CC.  
495 Taking into account soil combustion, we reach a value of 1.147 ( $\pm$  0.615) MtCO emitted into the atmosphere. BGS combustion  
496 dominates the total CO emissions, representing 87.3 ( $\pm$  0.8) % of the annual emissions. We also note that the Atlantic pine  
497 forest region, through the combustion of its SOM and lignite, accounted for 81.6 ( $\pm$  0.6) % of the CO emissions. In stark  
498 contrast, GFAS provided markedly lower CO emissions with 0.204 MtCO emitted during the 2022 fire season, which is 3 to  
499 8 times lower than our estimates when excluding belowground combustion, depending on the minimum and maximum values  
500 on CC and other emission parameters in table 2.

## 501 **4 Discussion**

### 502 **4.1 Remote sensing fire characterization for carbon emissions : beyond burned area**

503 Remote sensing information has played a key role in advancing our understanding of fire characteristics and their effects.  
504 Various studies have employed remote sensing data to examine various aspects such as estimates of burned areas (Chuvienco  
505 et al., 2019), fire sizes derived from aggregating burned pixel (Andela et al., 2019; Artés et al., 2019; Laurent et al., 2018,  
506 2019), fire spreading patterns based on burn dates within fire patches (Benali et al., 2016; Chen et al., 2022; Cardil et al.,  
507 2023), fire intensities determined by fire radiative power (Wooster et al., 2021), and fire severity assessment (Alonso-González  
508 and Fernández-García, 2021). While these advancements provide valuable insights to characterize key features of fires driving  
509 combustion and carbon emission processes, it is important to acknowledge their limitations. These include the difficulty in  
510 detecting small fires, which can lead to an underestimation of burned areas (cf. Mouillot et al., 2014 for review), as well as  
511 challenges in accurately assessing fire intensity (Freeborn et al., 2014). Additionally, uncertainties persist in detecting burned  
512 areas in the forest understorey (Roy et al., 2006), as well as in soils, peatlands (Atwood et al., 2016) and croplands (Hall et al.,  
513 2021). Combining information from both soil and vegetation fire types (Fisher et al., 2020; Sirin and Medvedeva, 2022) also  
514 remains a complex task. Efforts are currently underway to address these limitations through the development of more refined  
515 methods. These improvements encompass obtaining finer resolution data for burned area (Chuvienco et al., 2022), enhancing  
516 the detection of understorey fires (East et al., 2023), and providing more frequent and higher-resolution FRP datasets, such as  
517 those from VIIRS or stationary FRP information (Mota and Wooster, 2018). The use of hyperspectral sensors is also anticipated  
518 to offer new opportunities for improved fuel mapping, fire severity assessment and combustion analysis (Veraverbeke et al.,  
519 2018).

520 Based on current remote sensing strengths and weaknesses in fire characterization, we employed here the most detailed  
521 available data on burned areas and aboveground biomass in France. This fine-resolution dataset shows significant differences  
522 in burned estimates when compared to coarser resolution information (Vallet et al., 2023). We augmented this dataset with  
523 additional information on fire intensity, duration and ROS, all of which were calculated from 6-hourly VIIRS FRP data, as has  
524 been done in previous studies in different regions (Benali et al., 2016; Chen et al., 2022; Cardil et al., 2023).



525 An interesting addition to our analysis was the estimation of fire ROS, which exhibited considerable variability. ROS ranged  
526 from 1.7 km.h<sup>-1</sup> in Brittany, predominantly affecting heathlands, to 0.7 km.h<sup>-1</sup> in the Mediterranean basin, and even reached  
527 a significantly lower level in les Landes not exceeding 0.2 km/h. Our estimates of fire spread fall within the range of previous  
528 ROS estimates, which have varied from 0 and 30 km.day<sup>-1</sup> (equivalent to 0-1.25 km.h<sup>-1</sup>) in California (Hantson et al., 2022),  
529 with notable impacts observed when ROS exceeds 0.8 km.day<sup>-1</sup> and intensity surpasses 0.8MW. For instance, Cardíl et al.  
530 (2023) estimated ROS values of 0.12, 0.17, and 0.19 km.h<sup>-1</sup>, respectively for heathland, broadleaves, and pine forest based on  
531 hotspot data, while Salis et al. (2016) utilized fire spread models to estimate ROS ranging from 0.12 to 3.6 km.h<sup>-1</sup>. However,  
532 higher ROS have been observed in grasslands, ranging from 1.6 to 17 km.h<sup>-1</sup> (Cruz et al., 2022). Mediterranean fires are  
533 known to be predominantly wind-driven in southern France (Ruffault and Mouillot, 2015), resulting in fast and unidirectional  
534 fire spread patterns, which limits long fire residence time affecting soils. The northern region of France is windy on the Britany  
535 coast and northern Channel shores, but wind speed remains lower across the southwest (Landes). Additionally, the Atlantic  
536 influence of fast-moving low-pressure systems going from West to East leads to daily changes in wind directions, as opposed  
537 to the long-lasting unidirectional Mistral winds along the Mediterranean coast (Soukissian and Sotiriou, 2022). A noteworthy  
538 aspect related to intensity  $I$  (in MJ) is its relationship with heat release  $H$ , fuel consumption  $w$ , and rate of spread  $R$  (Alexander  
539 and Cruz, 2012). For a given intensity and heat release, fuel consumption is inversely related to ROS due to increasing  
540 residence times. This relationship suggests that slower fires may be more prone to consume larger fuel loads (Cobian-Iñiguez  
541 et al., 2022).

542 Regarding peatlands, previous studies have reported varying ROS values, with Cardíl et al. (2023) referring to 0.12 km.h<sup>-1</sup>  
543 based on remotely sensed hotspots, while Huang and Rein (2017) only report 10 cm.h<sup>-1</sup>. This indicates that hotspots over  
544 peatland might represent the flaming of the surface, whereas the actual combustion of peat and fire progression occurs at a  
545 much slower pace and with lower intensity, making it challenging to fully capture by thermal anomalies.

546 In summary, our exploration of fire spread processes in France has shown that the duration of hotspots within fire patches  
547 could serve as an effective and near-real-time indicator of soil combustion, which is closely related to smoldering combustion,  
548 and, in turn, shown by the low MCE values. This information on hotspot duration within fire patches has the potential to  
549 provide early warning signals for both populations and stakeholders, alerting them to potential air quality issues and the  
550 possibility of reignition (Xifré-Salvadó et al., 2020). Additionally, we recommend including this information as an additional  
551 key variable describing fire events in global fire patches databases (Laurent et al., 2018).

## 552 **4.2 Pre-fire carbon stocks uncertainties**

553 In addition to assessing the extent of burned areas, the accuracy of carbon emissions estimates is contingent upon the precision  
554 of the available biomass available for combustion. Recent enhancements in tree density and biomass estimation, encompassing  
555 isolated trees (Brandt et al., 2020) and more refined tree height data from Lidar (Schwartz et al., 2023), have played a crucial  
556 role in improving the reliability of such estimates. These advancements, which we incorporated into our methodology, have  
557 been discussed in Vallet et al. (2023).

558 Estimates of SOM at regional and global levels (Lin et al., 2022; Vanguelova et al., 2016) have historically exhibited a  
559 relatively large level of uncertainty. We decided to rely on the ESDAC database (Yigini and Panagos, 2016), a strategy  
560 consistent with SOM observations available across the country (Martin et al., 2019). It is worth noting that deeper soil  
561 conditions better correspond to soil carbon information derived from biogeochemical models (Van Der Werf et al., 2017; Van  
562 Wees et al., 2022).

563 Exploring the effects of fires on the depth of soil burning has been a relatively understudied domain at a large scale. There is  
564 potential for improvements through Lidar technology, which enables the identification of changes in soil surface thickness  
565 resulting from combustion (Reddy et al., 2015; Mickler et al., 2017), including low-severity peat fires (Bourgeau-Chavez et  
566 al., 2020). Peatlands, with their substantial stores of SOM, are susceptible to vertical spread rates, estimated at around  $1 \text{ cm.h}^{-1}$   
567 <sup>1</sup> by Huang and Rein (2017), or approximately  $0.8 \text{ cm.h}^{-1}$  ( $0.-2.3 \text{ cm.h}^{-1}$ ) in tropical peatlands (Graham et al., 2022). To maintain  
568 a conservative approach, we adopted a maximum ROS of  $0.2 \text{ cm.h}^{-1}$  for soil combustion, resulting in a daily consumption of  
569 approximately 4.8 cm, which roughly corresponds to 40 cm burned over an 8-day period, which corresponds to the average  
570 flaming duration of our fires. We computed peatland carbon stocks over a 2m depth, with a combustion completeness CC  
571 varying between 0.05 and 0.2, thus affecting between 10 cm and this maximum value of 40 cm. This range of values of  
572 consumed peat aligns with conventional peatland emissions models, often assuming 20 to 30 cm of peat being burned  
573 (Kohlenberg et al., 2018). However, it is worth noting that these parameters can vary from 1 cm to 54 cm in temperate peatlands  
574 in the UK (Davies et al., 2013). With this range of parameters, we reached an estimated carbon emission of  $172 (\pm 74) \text{ tC.ha}^{-1}$   
575 emitted (for a mean CC of 0.125 corresponding to 25 cm), which is higher than the value of  $96 \text{ tC/ha}$  estimated by Davies et  
576 al. (2013) for US temperate forests. For a comparative perspective, Mickler et al. (2017) using fine resolution LIDAR data  
577 revealed that temperate peatland wildfires could exhibit an average burn depth of 42 cm, resulting in an average belowground  
578 carbon emissions estimated at  $544.43 \text{ t C ha}^{-1}$ , highlighting the remain uncertainty on the combustion of these carbon pools  
579 for temperate forest. In terms of peatlands cover referencing in France, the Corine Land Cover (CORINE Land Cover 2018,  
580 2023) was utilized to identify their exposure to fires. According to this source, the extent of wetland (marshland and peatland)  
581 in France stands at around 89,000 ha. However, we note here that this information remains highly uncertain, with different  
582 estimates varying between 275,000 ha and 300,000 ha according to Tanneberger et al. (2017). This peatland extent would  
583 represent 0.52% of the country, out of which, 75,000 to 100,000 ha are considered as mires. For another comparison point,  
584 Muller (2018) estimated the extent of french peatland at 59,000ha, adding up uncertainty on the potential carbon emission  
585 from these fires under future climates and potential expansion of the pyroregions.

### 586 **4.3 Atmospheric assessments of combustion**

587 In addition to bottom/up approaches that rely on land surface combustion models and Earth observations, atmospheric fire  
588 emissions can also benefit from remote sensing methods for detecting fire plumes and assessing their CO concentrations, as  
589 demonstrated by the TROPOMI sensor (Zhou et al., 2022). This remote sensing data can be correlated with FRP (Griffin et  
590 al., 2023) and combustion efficiency (Van Der Velde et al., 2021). While it is important to validate this satellite data with

591 actual atmospheric measurements, it offers valuable insights to study the impact of fire events (Yilmaz et al., 2023). Recent  
592 developments in this field (Vernooij et al., 2022) include the use of Unmanned Aerial Vehicles (UAVs), primarily applied to  
593 grasslands and savannas. This approach is particularly promising for assessing the seasonal variability of emission factors  
594 (Vernooij et al., 2021). However, this measurement technique is restricted over forests, especially in Europe, where safety  
595 rules prevent the operation of aircraft or UAV's during firefighting interventions.

596 Our findings underscore that atmospheric tower measurements, while currently underutilized, represent an efficient and  
597 consistent surrogate, particularly for CO emissions (Wiggins et al., 2021). We have demonstrated the critical role of MCEs  
598 captured by the atmospheric mixing ratios in detecting smoldering combustion. Leveraging this information, we have enhanced  
599 the existing fire emissions assessments for Europe under the Copernicus framework using the GFAS protocol (Kaiser et al.,  
600 2012). This enables our bottom-up approach to be confronted and evaluated against tower-measured MCEs, an independent  
601 approach to detect and identify fire behaviors.

602 The routine integration of these atmospheric data in future research holds the potential to unveil temporal patterns of flaming  
603 vs. smoldering combustion within fire events and across different seasons, in line with recent observations collected across  
604 various ecosystems (Carter et al., 2020; Zheng et al., 2018). Such an endeavor requires atmospheric inversion modeling due  
605 to the distance from the actual combustion source, with plume dynamics influenced by wind direction, which could introduce  
606 uncertainties related to meteorological data (Challa et al., 2008). Additionally, further investigations into emissions factors for  
607 other greenhouse gases in the context of distinct fire types are warranted.

#### 608 **4.4 The 2022 fire-induce carbon emission budget**

609 In our study, we took the year 2022 as a reference, a year marked by significant fire events in various ecosystems across  
610 France, which are representative of Western Europe. A previous analysis conducted by Vallet et al. (2023) had already noted  
611 a substantial increase in biomass loss during 2022 in France; primarily due to an expanded burned area across the country.  
612 However, those conclusions were somewhat mitigated by the significant contribution of the low aboveground biomass affected  
613 by fires in Mediterranean shrublands and young managed forests in Les Landes. It is worth noting that this previous study  
614 provided an estimate solely for potential aboveground biomass loss.

615 In our research, we extended the analysis to account for soil combustion, which we identified through MCE measurements  
616 from atmospheric towers. Consequently, our findings suggest that  $7.95 (\pm 3.63)$  MteqCO<sub>2</sub> were emitted into the atmosphere  
617 during the 2022 fire season. Notably,  $54.3 (\pm 9.9)$  % of these emissions originated from the belowground biomass, with  $35.4$   
618  $(\pm 10.4)$  % from peat and SOM, and  $18.95 (\pm 0.65)$  % from lignite. These latter processes are often overlooked in fire emissions  
619 assessment. In comparison, our estimates are 2-fold higher than the GFAS estimate of 4.18MteqCO<sub>2</sub> (CO and CO<sub>2</sub>), which  
620 excludes these processes in temperate forest.

621 Consequently, fire represents a huge source of greenhouse gases. Considering that the national carbon footprint amounted to  
622 403,8 MteqCO<sub>2</sub> in 2022, fire represents 1.97 % ( $\pm 0.89$ ) of french emissions of greenhouse gases into the atmosphere (Citepa,

623 2023). Moreover, as forest is estimated to sequester 27 MteqCO<sub>2</sub> per year in the country, fire disturbance would represent a  
624 reduction of 30 % in this carbon sink for this particular year.

625 One remarkable aspect of 2022 fire season was the distinct impact on vegetation types (broadleaf vs. needle leaf), with varying  
626 rates of soil carbon accumulation. Temperate forests, characterized by a slower decomposition rate compared to the warmer  
627 Mediterranean climate, harbor more substantial litter and SOM density (Kurz-Besson et al., 2006). Additionally, our analysis  
628 revealed that the 2022 fires affected 510 ha of peatlands, as referenced in the Corine Land Cover dataset, contributing to 2.6 -  
629 3.9% of the total carbon emitted.

630 While carbon stock associated with charcoal or lignite is often ignored, located beneath the SOM layer, we demonstrated here  
631 that this contributor is significantly impacted during this unusual fire season. This particular combustion impacted 2,265 ha  
632 over the lignite mines in Les Landes, a phenomenon reported by local authorities and substantiated by our low MCE  
633 measurements. These low MCE values, which are challenging to account for based on biomass or SOM combustion alone,  
634 indicate the occurrence of lignite fires that could take place over an extended period. This phenomenon, reminiscent of the  
635 ‘zombies’ fires recently observed, has been reported by local authorities to have lasted even longer than expected over the  
636 winter 2022-2023 (McCarty et al., 2021; Irannezhad et al., 2020; Scholten et al., 2021; Kuklina et al., 2022). While lignite  
637 fires remain infrequent and typically omitted in carbon emissions inventories, they have been documented in other parts of the  
638 world (Stracher and Taylor, 2004; Brown, 2003; Fredriksson, 2004). These fires should raise concerns from authorities with  
639 additional preventive measures in France, especially in areas with superficial lignite deposits and accumulated carbon residues  
640 from historical charcoal basins, some of which have grown to a substantial height of 100m in northern France (Anon, 2023).  
641 Hotspot thermal anomalies and reignitions may persist up to three weeks after a fire, potentially emitting more carbon than our  
642 direct estimates suggest. These emissions, however, may be of a long-lasting nature but with a low intensity below the detection  
643 level of detection methods using atmospheric mixing ratios. Therefore, it is advisable to establish a more comprehensive  
644 measurement network to better understand and to document this unexplored aspect of fire impact across European temperate  
645 forests.

646 Our results, while providing a preliminary and potentially conservative assessment of soil combustion in the region, underscore  
647 the need for enhanced field assessments of fire-induced effects on soil carbon stocks, particularly in peatlands and pine forests.  
648 These impacts could be even more substantial than initially calculated, emphasizing the importance of further investigation.

#### 649 **4.5 Future directions for soil combustion modeling in Europe**

650 Our investigation into fire emissions during the 2022 fire season in France carries significant insights that can be extended to  
651 applications across the entire European continent. Current global fire emission assessments, such as GFED, GFAS, and FINN,  
652 predominantly focus on the combustion of deep SOM in boreal regions and specific tropical peatlands. In contrast, regions  
653 like European temperate forests and, by extension, our study area, are generally assumed to leave the soil unaffected by fire,  
654 except for litter burning (Van Wees et al., 2022).

655 One limitation in existing greenhouse gas emission inventories from fires is the failure to adequately account for the transition  
656 between the flaming and smoldering phases in aboveground biomass combustion. Following a study on fire emissions in  
657 California, Mebust et al. (2011) cautioned that current emission factors might overestimate the contribution of flaming  
658 combustion while underestimating the significance of smoldering combustion in total fire emissions. This concern was also  
659 raised by Garcia-Hurtado et al. (2013) in Europe, who estimated that 25% of emissions were associated with flaming and 75%  
660 with smoldering. Our approach sought to address this limitation by considering these different combustion phases in our  
661 processing chain.

662 A second limitation in current carbon emission inventories pertains to the SOM accumulation and combustibility, which may  
663 have been previously underestimated. Recent studies have identified significant instances of smoldering combustion in areas  
664 where it was not previously considered, such as China's temperate forests (Tang et al., 2023) and even in African savannas  
665 towards the end of the burning season (Zheng et al., 2018). While temperate forests, characterized by milder temperatures and  
666 seasonal variations in soil moisture, were traditionally assumed to accumulate less carbon in soils compared to boreal forest,  
667 the actual situation is more nuanced. SOM levels (but also bulk density allowing for oxygen transfer and better combustion)  
668 can vary locally in Europe, depending on factors like local climate and specific soil and leaf types. These traits, such as pH  
669 (Xiang et al., 2023) and leaf types (needles vs. broadleaves) can influence decomposition rates (Masuda et al., 2022; Krishna  
670 and Mohan, 2017; Cornelissen et al., 2011), highlighting the potential of using key plant traits as surrogates for SOM  
671 assessment. While SOM databases remain somewhat uncertain (Lin et al., 2022) insights from plant traits can be valuable.

672 The assumption that Mediterranean soils have been widely reported to hold low carbon stocks, thus not contributing to carbon  
673 emissions during fires, might not apply uniformly. For example, Certini et al. (2011) report that most carbon losses in  
674 Mediterranean pine forests (Tuscany, Italy) are attributable to the elimination of the litter layer, rather than changes in the  
675 underlying mineral soil carbon content ; a conclusion also supported by Almendros and González-Vila (2012). This assumption  
676 might be true for broadleaf forests and shrublands, representing a large portion of burned area in Europe. However, smoldering  
677 combustion has been reported in some Mediterranean pine forests in Spain (Prat-Guitart et al., 2016), central European scots  
678 pines, and in California for upper and lower duff (Garlough and Keyes, 2011), with moisture thresholds of 57% and 102%  
679 (Hille and Den Ouden, 2005). Our study confirmed smoldering combustion in temperate Pine woodlands and heathlands.  
680 Therefore, we suggest that plant species distribution, and their leaf traits like pH and leaf type could be used to identify  
681 locations with substantial SOM accumulation, potentially leading to soil smoldering phases that should be included in carbon  
682 emission models. Notably, in higher latitudes (Turetsky et al., 2011b; Mekonnen et al., 2022; Walker et al., 2020) and eastern  
683 EU regions (Kirkland et al., 2023), carbon emissions from soil combustion can account for up to 90% of the total carbon  
684 emitted. This has implications for the refinement of air quality estimates, which often rely on emissions derived from standard  
685 remote sensing information and models (Menut et al., 2023).

686 We recommend the initiation and compilation of an emission factor inventory over Europe, following initiatives in the US and  
687 Canada (Prichard et al., 2020). Additionally, considering duff peat emissions and making more extensive use of the  
688 atmospheric tower network and fine temporal resolution remote sensing would enhance our understanding of fire events. Based

689 on the boreal and tropical experience, peatland moisture content appears to be a critical factor influencing combustion depth  
690 and emission factors. Smoldering of biomass at lower moisture contents develops wider pyrolysis fronts that release a larger  
691 fraction of other gas species (Rein et al., 2009). Pyrolysis can even reach very low MCEs with large CO emissions (Song et  
692 al., 2020; Kohlenberg et al., 2018) when temperatures reach above 400 °C. Comprehensive models should integrate on-site  
693 peat and SOM moisture to account for changes in combustion rate and emission factors. This information has been available  
694 in France since 2016 through the peatland observation network (Bertrand et al., 2021; Gogo et al., 2021).  
695 Understanding and predicting SOM and peat fire ignition and spread in temperate forests remain relatively unexplored areas  
696 of research due to the limited number of fire events as case studies. For instance, the ignition probability for SOM layers and  
697 peatlands is actually not yet fully comprehended. Pine cones have been identified as potentially influencing the ignition of soil  
698 duff (Kreye et al., 2013), thereby favoring smoldering, which is particularly relevant given that coniferous ecosystems tend to  
699 accumulate more SOM. Moreover, the spread of smoldering combustion is not well represented in current fire models, and its  
700 link with duff depth is minimal (Miyaniishi and Johnson, 2002). The overall consequences of soil smoldering combustion  
701 extend beyond carbon emissions, affecting ecological factors, such as the regeneration potential of seeder species like pines  
702 (Madrigal et al., 2010, Watts and Kobziar, 2013). Consequently, we echo the conclusion reached by Xifré-Salvadó et al. (2020)  
703 that SOM and peatland fires in France and European temperate forests should be more deeply considered in terms of wildfire  
704 hazard, in particular for re-ignitions. For instance, the Landiras1 fire exhibited smoldering combustion for 10 days before  
705 reigniting from its south-western part over the lignite fires to ignite the Landiras 2 fire. Moreover, soil fires should be accounted  
706 for in forest planning and management, including soil fuel breaks strategies to halt smoldering combustion (Lin et al., 2021),  
707 in addition to the conventional focus on canopy fuel breaks.

## 708 **5 Conclusion**

709 This study offers compelling direct evidence of variable smoldering combustion rates observed during the atypical 2022 fire  
710 season. We employed the Modified Combustion Efficiency ratio, with atmospheric CO<sub>2</sub> and CO concentrations, calculated  
711 using data from the greenhouse gas atmospheric tower network situated throughout France. This particular year witnessed a  
712 significantly higher extent of burned area in the temperate Atlantic forest, marking a critical study case encompassing all major  
713 French sylvo-regions. Our findings allow us to draw several important conclusions :  
714 First, we provided empirical support for the occurrence of soil, peatland and even deeper lignite fires, phenomena that have  
715 previously been insufficiently demonstrated or evaluated through remotely sensed burn area data.  
716 Second, we highlighted the large contribution of these fires within the overall carbon emission budget and trace gas emissions,  
717 which have not been fully integrated into existing fire emissions models.  
718 Lastly, our study enabled us to propose valuable warning signals for assessing re-ignition hazards and developing post-fire  
719 management strategies based on the duration and intensity of hotspots within the affected area and atmospheric tower data.

720 This research serves as a stepping stone for the development of future fire impact warning systems and emphasizes the potential  
721 of utilizing atmospheric greenhouse gas measurements in fire impact assessments. We also stress the need for enhanced  
722 vegetation and soil carbon emissions factors during both flaming and smoldering phases. Finally, we advocate for efforts on  
723 updating and further validating, from top-down approaches, fire emissions processing chain for European temperate forests.

#### 724 **Data availability**

725 Fire model emissions are available through the OSU OREME website.

726

727 Financial support.

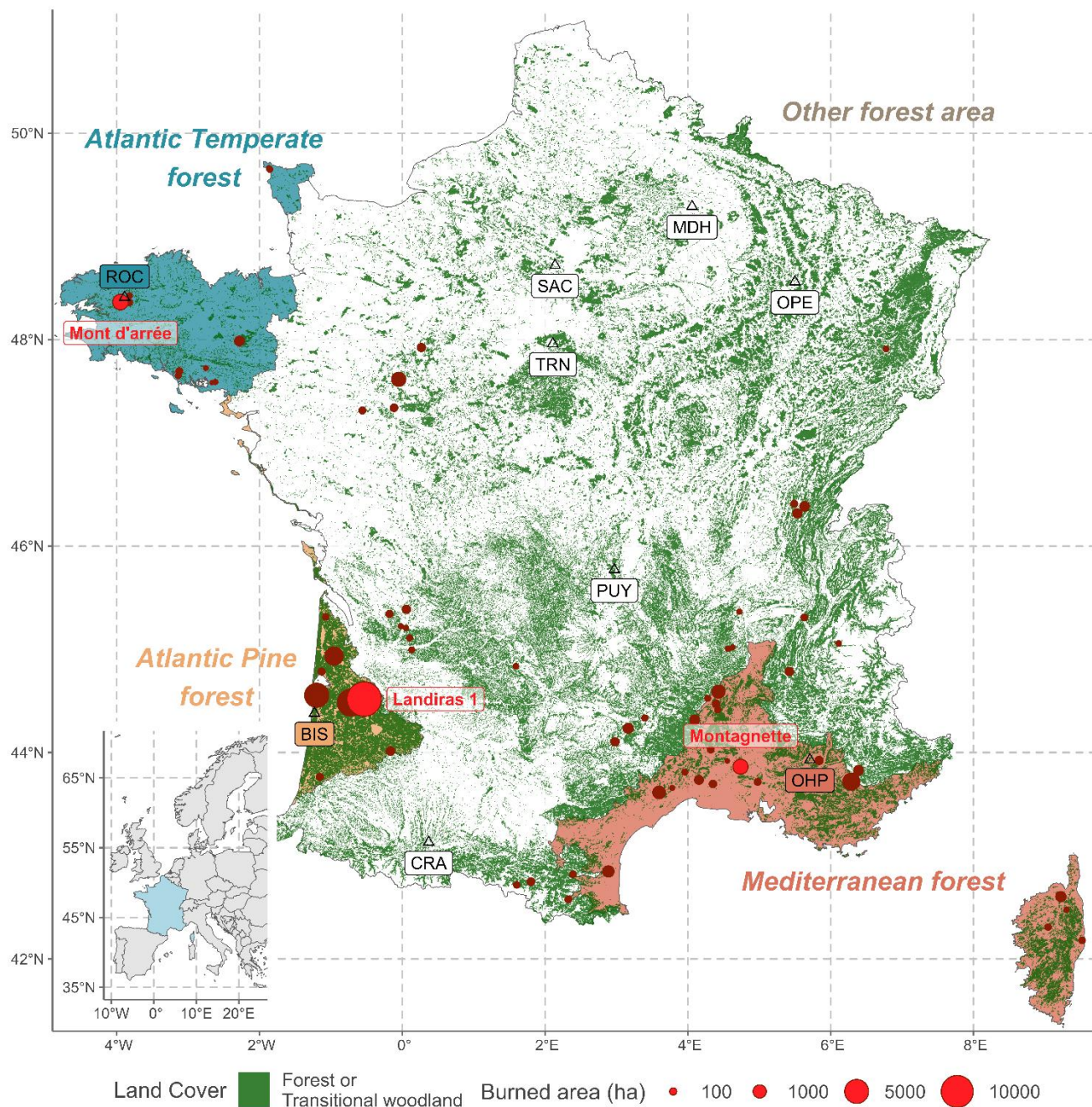
728 This work was supported by the French Environment and Energy Management Agency (ADEME), the FirEUrisk H2020  
729 project and the OSU OREME. The FirEUrisk project has been granted funding from the European Union's Horizon 2020  
730 research and innovation program under grant agreement no. 101003890. This work was also supported by the Climate Change  
731 Initiative (CCI) Fire\_cci Project (contract no. 4000126706/19/I-NB).

#### 732 **Author contributions**

733 LV, FM and TL supervised the study framework. LV performed data curation and analysis on the fire emission model. LV,  
734 FM and PC assembled the fire emission model and parameters. CA, LJ and TL performed mixing ratios analysis. MR, ML  
735 and IXR provided data from the atmospheric towers. LV, FM and CA wrote the manuscript. All authors revised the manuscript.

#### 736 **Competing interests**

737 The contact author has declared that none of the authors has any competing interests.



738

739

740

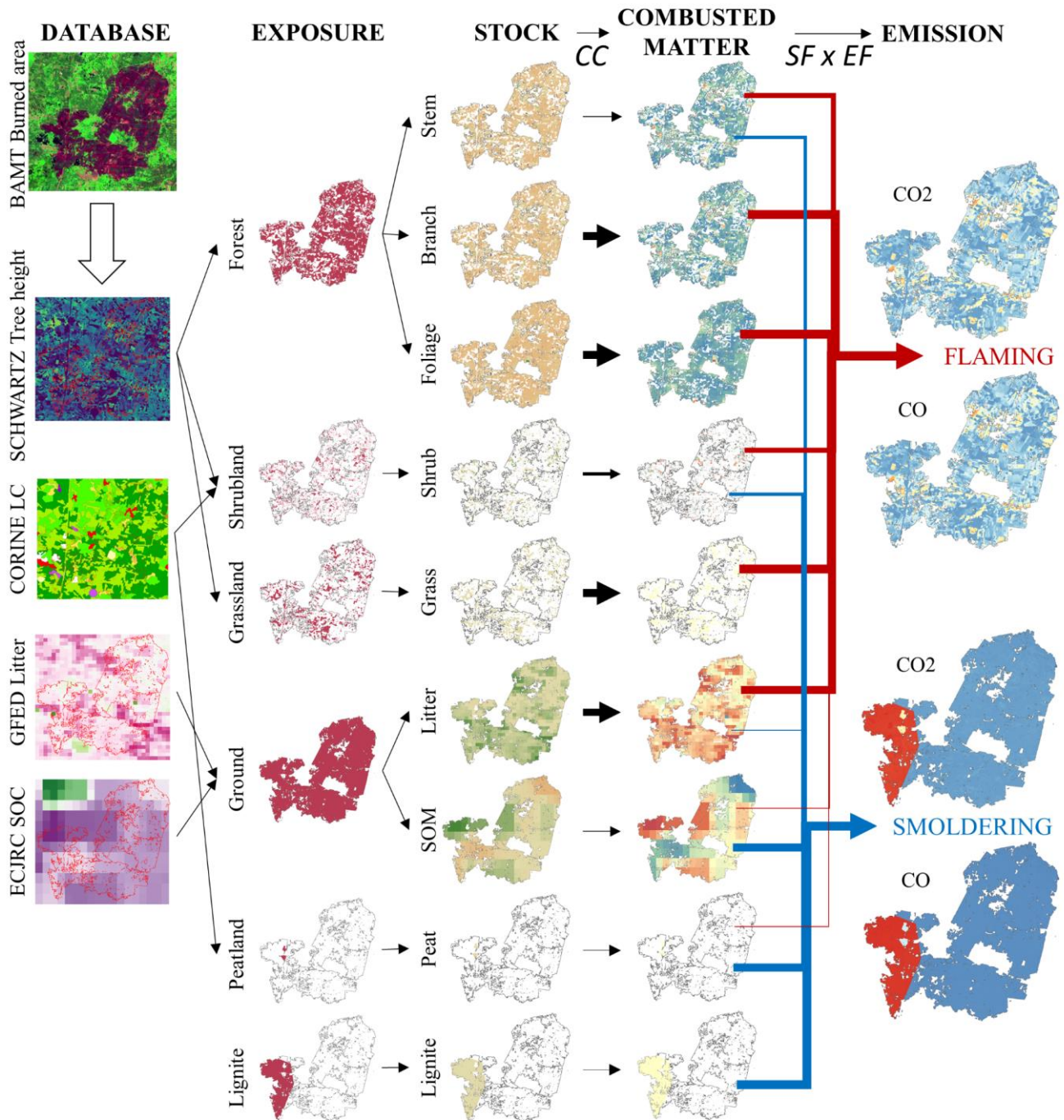
741

742

743

**Figure 1.** Map of the French forests with the location of fires larger than 30 ha that occurred in 2022 fire season. France is divided into four regions ('Atlantic Temperature forest', 'Atlantic pine forest', 'Mediterranean forest' and 'Other forest area') according to forest type (IFN, 2023b) and frequency of fire disturbance (BDIFF, 2023). The locations of the atmospheric towers (including ROC: Roc'h Trédudon, BIS: Biscarrosse, and OHP: Observatoire de Haute Provence) and the burned areas of the three corresponding main fires of interests are also represented ('Monts d'Arrée', 'Landiras 1' and 'Montagnette', red circles).

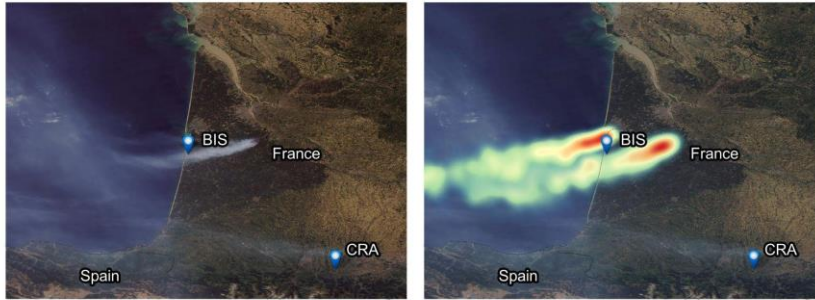




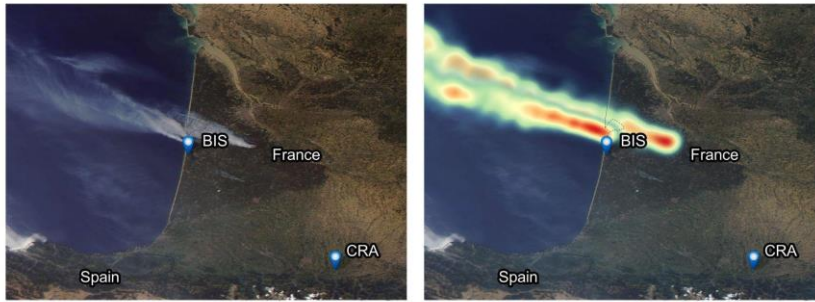
744  
745  
746  
747  
748  
749

Figure 2. Refined fire emission model for temperate forest. The processing chain takes initial datasets as inputs to obtain exposure (burned area affecting each pool) and pool estimation (total amount of dry matter located in the burned area). Through specific values of Combustion completeness (CC), Smoldering fraction (SF) and Emission factors (EF), the model calculate combusted matter (fraction of pool actually combusted) and emissions to the atmosphere (CO and CO<sub>2</sub>) in the flaming and smoldering phases (see Table 2).

2022-07-16



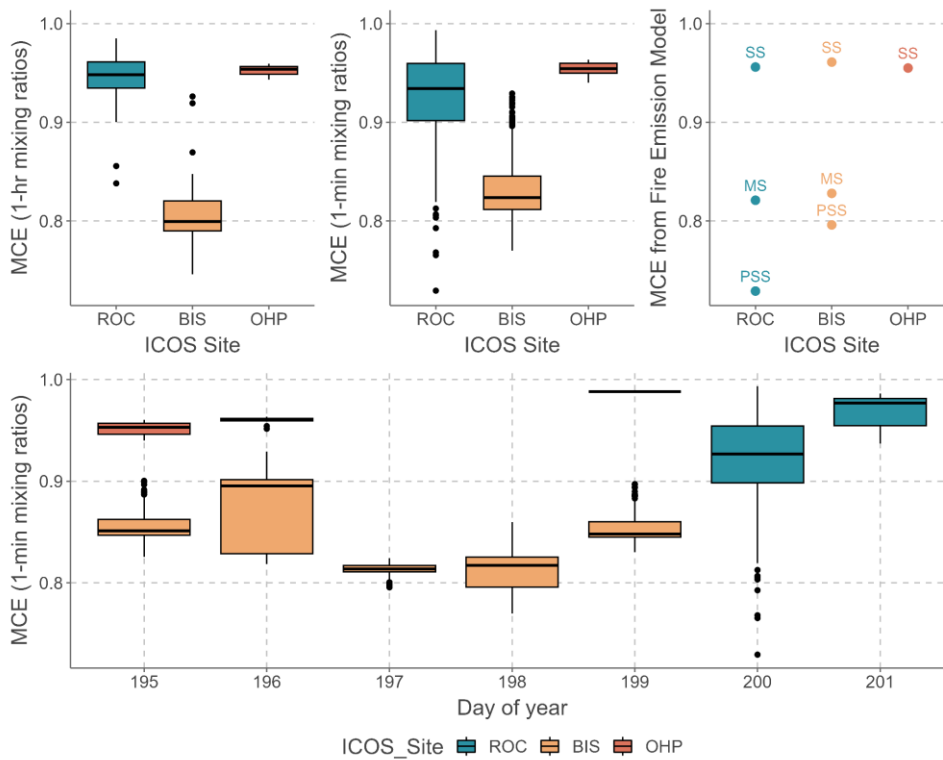
2022-07-18



750

751  
752

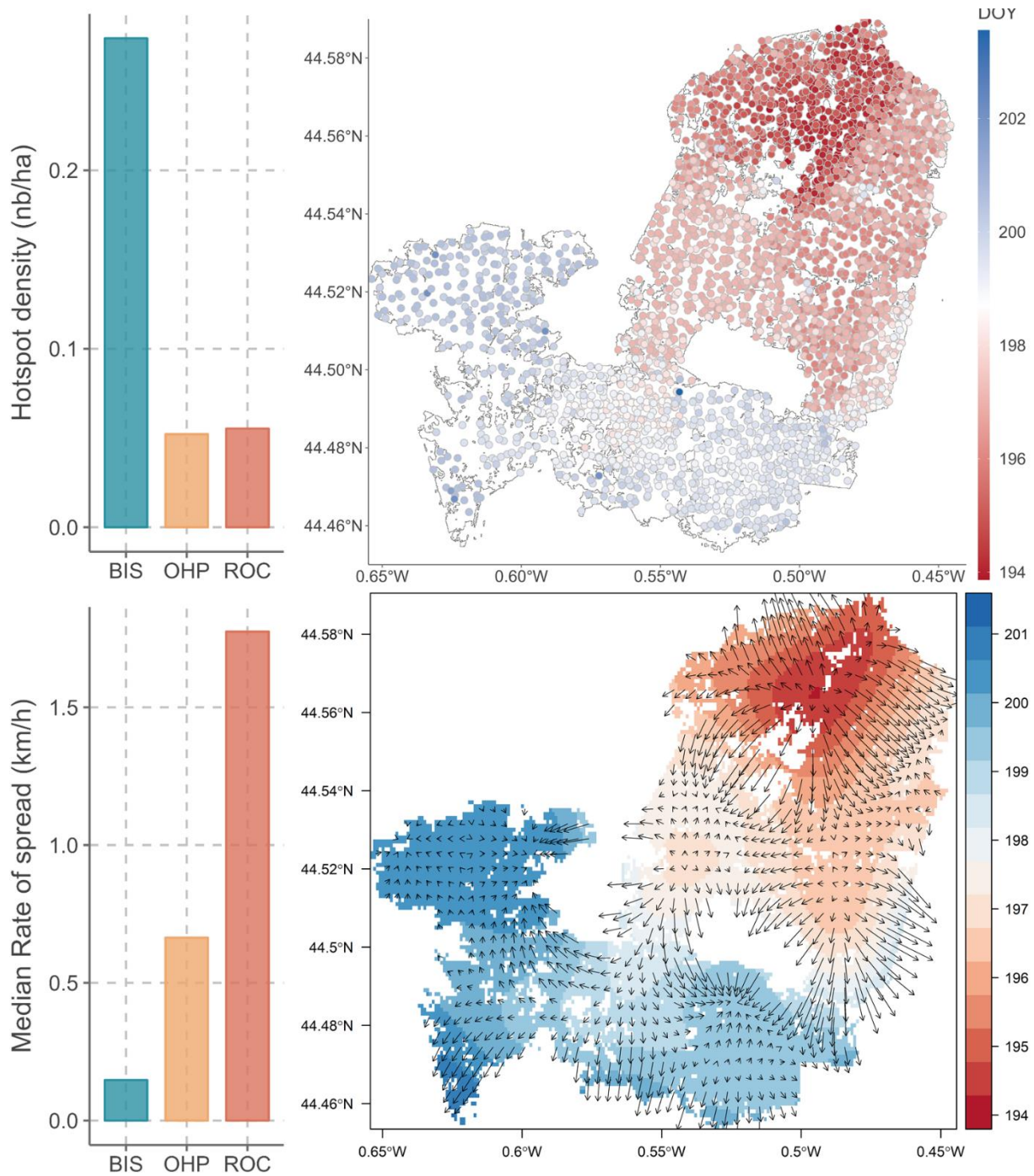
**Figure 3. Overlay of the MODIS (observed, left column) and the HYSPLIT (modeled, right column) plumes on 16 and 18 July 2022 during the Landes wildfires (red for the highest particle density, yellow for the lowest particle density).**



753

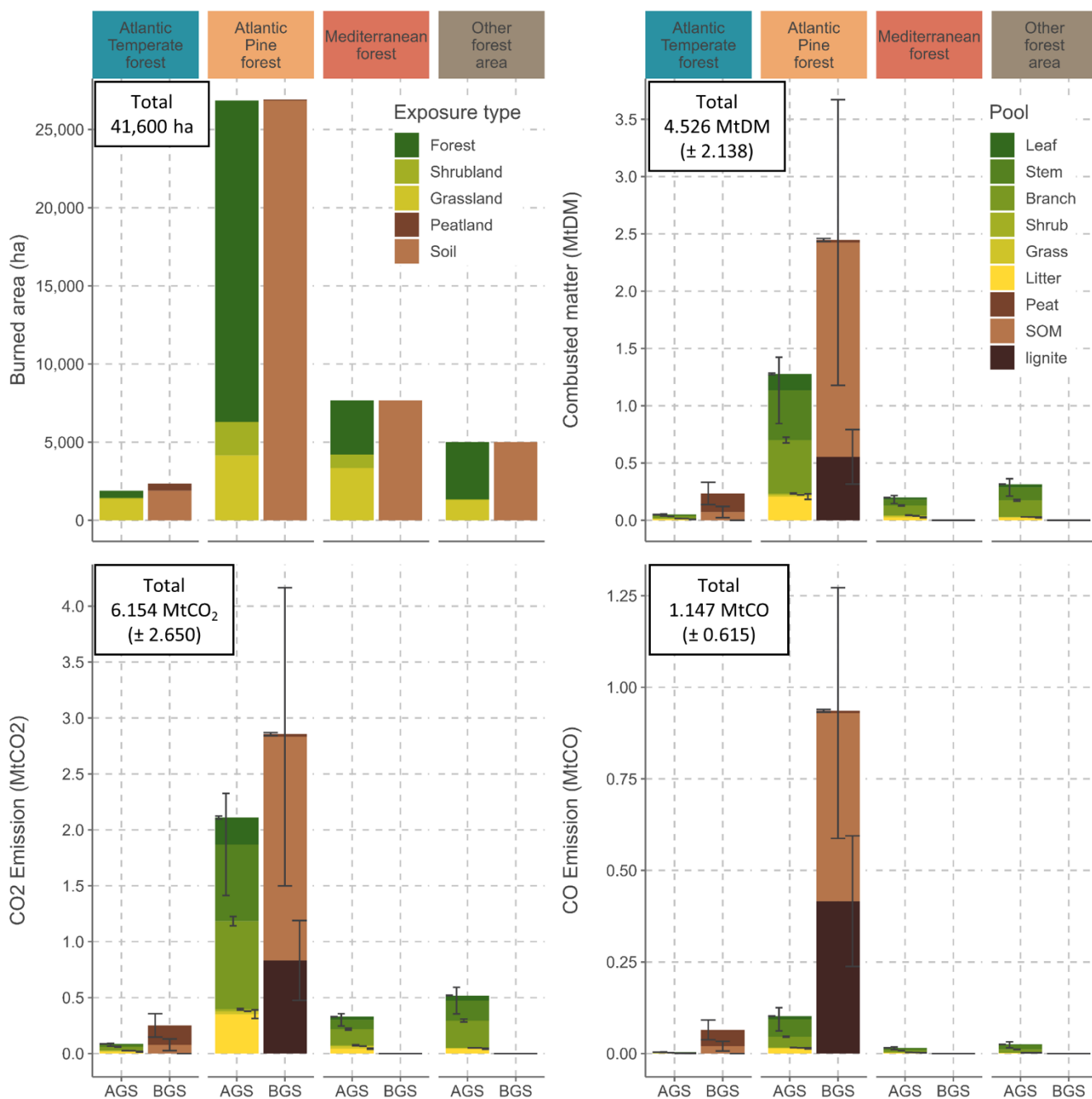
754  
755  
756  
757

Figure 4. Top : Median and quartiles of the Modified Combustion Efficiency (MCE) observed at the three atmospheric stations (ROC, BIS, OHP) impacted by the nearby fires Monts d'Arrée, Landiras1, and La Montagnette, respectively. The left graph shows 1-hour mixing ratios. The middle graph shows 1-minute mixing ratios. The right graph shows MCE obtained from the fire emission model (See Table 4). Bottom : Daily median and quartiles values of the same corresponding data for 1-minute mixing ratios.



758

759 **Figure 5. Top :** Hotspot density (nb.ha<sup>-1</sup>) for each main fire and its corresponding flux tower (BIS, OHP, ROC) and an example of  
 760 hotspot distribution on BIS fire (Landiras 1), with corresponding Day of Year (DOY). Bottom : Median fire spread (km.h<sup>-1</sup>) for each  
 761 main fire and its corresponding flux tower (BIS, OHP, ROC) and an example of interpolated fire spread on BIS fire. The color scale  
 762 indicates the day of the year of burning (decimal DOY) and arrows indicate the direction and rate of spread (proportional length of  
 763 the arrow). Ignition corresponds to the pixel with the earliest DOY. We observed the change in spread direction toward south-west  
 764 at first then moving west and north-west in accordance to changes in wind direction occurring during this fire (cf Fig. 3).



765

766 **Figure 6. National footprint of France for the 2022 fire season. The Burned area (ha), Combusted matter (MtDM), CO<sub>2</sub> and CO**  
 767 **(Mt) emissions are shown for each region, each stock type (AGS : Aboveground stock, BGS : Belowground stock) and each pool.**  
 768 **Values are provided in Table A1.**

769  
 770

771

772 **Table 1. Summary of the random forest model's performance across the atmospheric stations. The performance metrics are**  
 773 **coefficient of determination (R<sup>2</sup>) and root-mean-square error (RMSE). Tower location and height is also included.**

Tower short name	Location	Height (AGL, m)	RF performance			
			CO		CO <sub>2</sub>	
			R <sup>2</sup>	RMSE (ppb)	R <sup>2</sup>	RMSE (ppm)
BIS	44.38° N, -1.23° E	73	0.76	9.04	0.96	1.12
CRA	43.13° N, 0.37° E	60	0.76	9.05	0.96	1.35
MDH	49.24° N, 4.06° E	48	0.74	8.43	0.89	1.56
OPE	48.56° N, 5.5° E	50	0.77	7.18	0.96	1.22
PUY	45.77° N, 2.97° E	10	0.85	6.61	0.98	0.82
ROC	48.41° N, -3.89° E	80	0.85	5.85	0.98	0.65
SAC	48.72° N, 2.14° E	100	0.79	8.62	0.96	1.34
TRN	47.96° N, 2.11° E	50	0.79	6.41	0.96	1.16

774 **Table 2. Synthesis table of parameters used in the refined fire emission model. Minimum and maximum combustion completeness**  
 775 **(CC), smoldering fraction (SF) and emission factors (EF) for the smoldering (S) and flaming (F) combustion to CO and CO<sub>2</sub> are**  
 776 **based on previously reported values in the carbon emission scientific literature. Intrinsic MCE values (MCE<sub>i</sub>) calculated from Eq.**  
 777 **2 are also provided.**

Stock and pools	CC		SF	EF (g of gas per kg of DM pool)				MC Ei	references
	min	max		CO <sub>2</sub>		CO			
				F	S	F	S		
Aboveground stock (AGS)									
stem	0.10	0.50	0.40	1,700	1,400	73	165	0.935	(Van Wees et al., 2022; Prichard et al., 2020; Balde et al., 2023; Akagi et al., 2011)
branch	0.90	1.00	0.00	1,686		63		0.964	(Van Wees et al., 2022; Prichard et al., 2020)
leaf	0.90	1.00	0.00	1,686		63		0.964	(Van Wees et al., 2022; Prichard et al., 2020)
shrub	0.40	0.99	0.40	1,746	1,460	72	93	0.953	(Van Wees et al., 2022; Prichard et al., 2020; Akagi et al., 2011; Garcia-Hurtado et al., 2013)
grass	0.90	1.00	0.00	1,686		63		0.964	(Van Wees et al., 2022; Prichard et al., 2020)
litter	0.80	1.00	0.10	1,696	1,750	64	119	0.961	(Van Wees et al., 2022; Prichard et al., 2020)
Belowground stock (BGS)									
SOM	0.10	0.50	0.90	1,696	1,000	64	298	0.796	(Van Wees et al., 2022; Prichard et al., 2020)
peat	0.05	0.20	0.90	1,696	1,000	64	298	0.796	(Van Wees et al., 2022; Prichard et al., 2020; Akagi et al., 2011; Rein et al., 2009; Geron and Hays, 2013)
lignite	0	0	1.00		1,500		750	0,666	(Song et al., 2020)

0 0  
 1 2  
 5

779

780 **Table 3. Description of ROC, BIS and OHP fires in terms of exposure (ha of vegetation and soil types affected), pool dry matter**  
 781 **density (tDM.ha<sup>-1</sup>) for aboveground (stem, branch, leaf, shrub, grass, litter) and belowground (SOM, peat, lignite) pools, and the**  
 782 **resulting total pool dry mass actually affected by fire (tDM).**

	ROC	BIS	OHP
IGNITION DATE	18th July 2022	12th July 2022	14th July 2022
DURATION	2 days	10 days	2days
EXPOSURE (ha)			
fire	1,726	12,140	1,477
forest	129	8,622	1,124
shrubland	54	1,257	226
grassland	1,093	2,200	127
soil	1,276	12,078	1,477
peatland	449	61	
lignite		1,909	
POOL DENSITY (tDM.ha <sup>-1</sup> )			
stem	25.0	40.7	42.3
branch	8.5	13.8	14.4
leaf	12.9	5.7	3.7
shrub	7.8	7.3	10.0
grass	4	4	4
litter	5.0	7.3	3.8
SOM	140.1	235.7	95.2
peat	2,900.0	2,900.0	
lignite		14,000	
POOL DRY MASS (tDM)			
stem	3.22e+03	3.51e+05	4.75e+04
branch	1.10e+03	1.19e+05	1.62e+04
leaf	2.36e+03	5.61e+04	4.97e+03
shrub	4.23e+02	9.16e+03	2.26e+03
grass	4.43e+03	8.84e+03	5.21e+02
litter	6.34e+03	8.79e+04	5.64e+03
SOM	1.79e+05	2.85e+06	1.41e+05
peat	1.30e+06	1.77e+05	
lignite		2.67e+07	

797

798

799

800

801

802

803

804

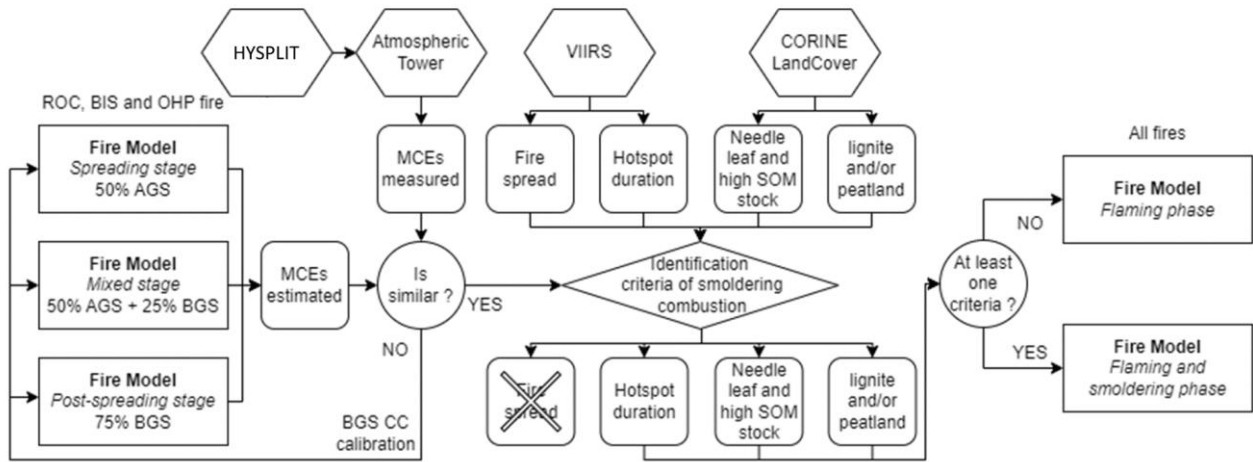
805

806  
807  
808  
809  
810  
811  
812  
813  
814

**Table 4. Bottom-up approach from stock to carbon emissions. Total pool dry matter combusted (tDM) and CO<sub>2</sub> and CO emissions (in g) estimates are based on parameters of Table 2. The resulting MCE is provided for each approach (considering only AGS or including also BGS), each fire and each combustion stage. AGS : Aboveground stock, BGS : Belowground stock, SS : spreading stage, MS : mixed stage, PSS : post-spreading stage.**

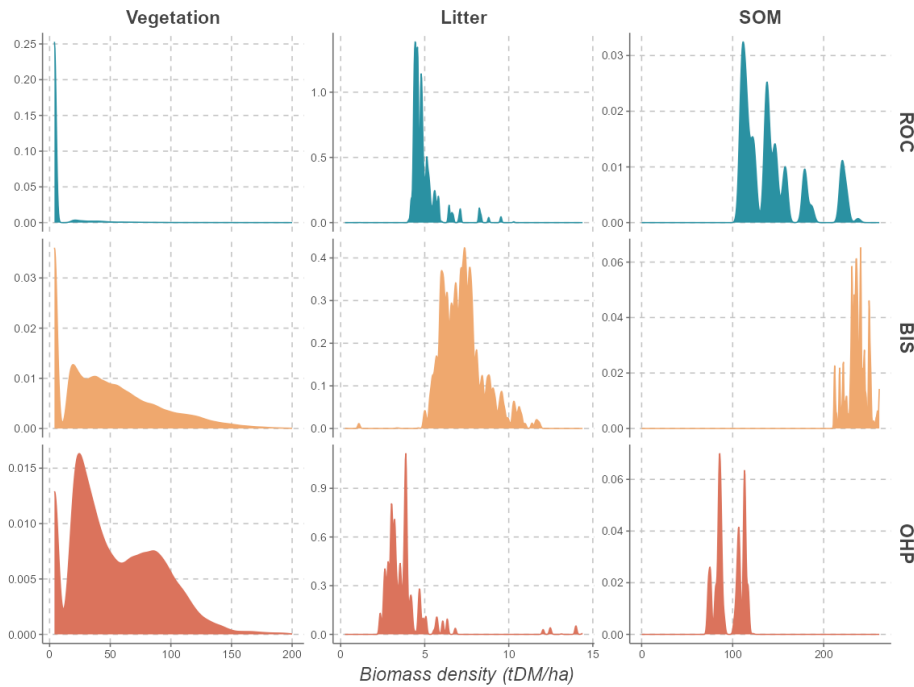
	<i>Stock type</i>	<i>Matter combusted (tDM)</i>	<i>Emission (g)</i>		<i>MCE</i>
			<i>CO<sub>2</sub></i>	<i>CO</i>	
<b>AGS ONLY</b>					
ROC	AGS	1.45e+04 (± 1.8e+03)	2.44e+10 (± 2.97e+09)	9.99e+08 (± 1.5e+08)	0.961 (± 0.001)
BIS	AGS	3.66e+05 (± 9.09e+04)	6.06e+11 (± 1.46e+11)	2.86e+10 (± 9.11e+09)	0.956 (± 0.004)
OHP	AGS	4.15e+04 (± 1.18e+04)	6.84e+10 (± 1.89e+10)	3.34e+09 (± 1.2e+09)	0.955 (± 0.004)
<b>AGS + BGS</b>					
<b>ROC</b>					
	SS				0.961 (± 0.001)
	AGS	7.23e+03 (± 8.99e+02)	1.22e+10 (± 1.48e+09)	4.99e+08 (± 7.49e+07)	
	MS				0.828 (± 0.015)
	AGS	7.23e+03 (± 8.99e+02)	1.22e+10 (± 1.48e+09)	4.99e+08 (± 7.49e+07)	
	BGS	5.41e+04 (± 3.34e+04)	5.79e+10 (± 3.57e+10)	1.49e+10 (± 9.16e+09)	
	PS				0.796 (± 0.001)
	S				
	BGS	1.62e+05 (± 1e+05)	1.74e+11 (± 1.07e+11)	4.46e+10 (± 2.75e+10)	
<b>BIS</b>					
	SS				0.956 (± 0.004)
	AGS	1.83e+05 (± 4.54e+04)	3.03e+11 (± 7.29e+10)	1.43e+10 (± 4.56e+09)	
	MS				0.821 (± 0.015)
	AGS	1.83e+05 (± 4.54e+04)	3.03e+11 (± 7.29e+10)	1.43e+10 (± 4.56e+09)	
	BGS	3.36e+05 (± 1.96e+05)	4.1e+11 (± 2.31e+11)	1.48e+11 (± 7.76e+10)	
	PSS				0.729 (± 0.011)
	BGS	1.01e+06 (± 5.87e+05)	1.23e+12 (± 6.93e+11)	4.44e+11 (± 2.33e+11)	





824

825 Figure A3. Fire model calibration process. AGS : Aboveground Stock, BGS : Belowground stock, MCE : Modified  
 826 Combustion Efficiency, SOM : Soil Organic Matter

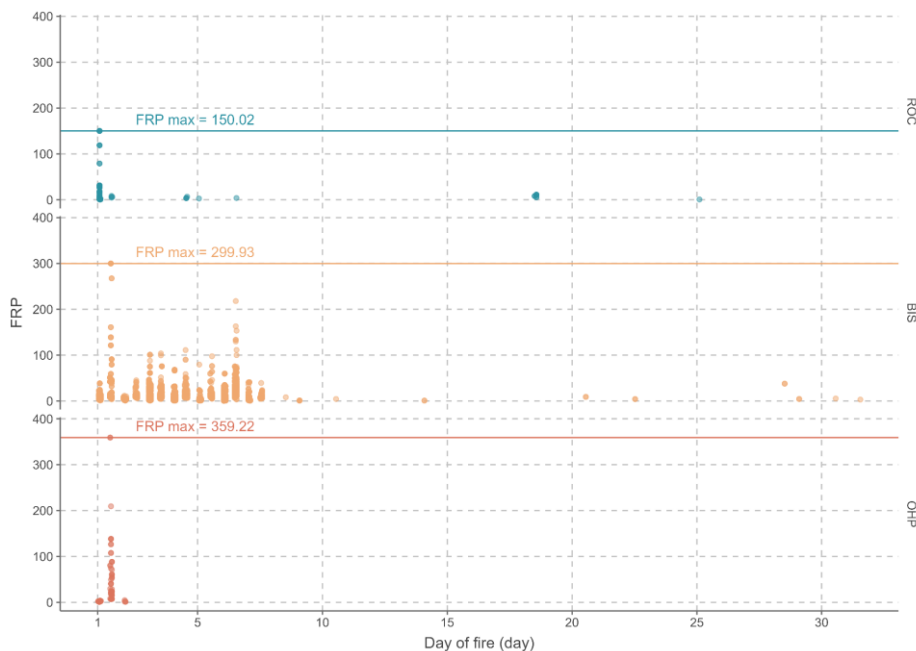


827

828

829

827 **Figure A2. Vegetation biomass (stem, branch, leaf, shrub and grass), litter and SOM density (tDM.ha-1) distribution for the BIS,**  
 828 **ROC and OHP fires.**



830

831 **Figure A3. VIIRS/MCD14ML Fire Radiative Power (FRP, in MW) temporal distribution from ignition to 5 weeks after ignition for**  
 832 **each ROC, BIS and OHP fires.**

833 **Table A1. Burned area (ha), Stock (MtDM), Matter combusted (MtDM), CO<sub>2</sub> and CO emissions (in Mt), resulting MCE, and GFAS**  
 834 **estimation in France for the 2022 summer fire season and for the 4 regions.**

Region	Burned area (ha)	Stock type	Stock (MtDM)	Matter combusted (MtDM)	Emission (Mt)		MCE	GFAS Emission (Mt)	
					CO <sub>2</sub>	CO		CO <sub>2</sub>	CO
Atlantic Temperate forest	2,315	AGS	0.081	0.052 (± 0.010)	0.086 (± 0.017)	0.004 (± 0.001)	0.841 (± 0.017)	0.155	0.007
		BGS	1.546	0.236 (± 0.146)	0.252 (± 0.156)	0.065 (± 0.040)			
Atlantic Pine forest	26,850	AGS	2.351	1.278 (± 0.350)	2.111 (± 0.559)	0.102 (± 0.036)	0.834 (± 0.015)	2.914	0.159
		BGS	38.121	2.447 (± 1.498)	2.856 (± 1.704)	0.936 (± 0.524)			
Mediterranean forest	7,600	AGS	0.332	0.199 (± 0.046)	0.330 (± 0.074)	0.015 (± 0.005)	0.957 (± 0.003)	0.272	0.014
		BGS	0.850						
Other forest area	4,839	AGS	0.590	0.315 (± 0.087)	0.519 (± 0.139)	0.025 (± 0.009)	0.955 (± 0.004)	0.516	0.024
		BGS	0.808						
<b>Total</b>	<b>41,600</b>		<b>44.680</b>	<b>4.526 (± 2.138)</b>	<b>6.154 (± 2.650)</b>	<b>1.147 (± 0.615)</b>	<b>7.172 (± 0.081)</b>	<b>3.857</b>	<b>0.204</b>

835

836 **References**

837 Akagi, S. K., Yokelson, R. J., Wiedinmyer, C., Alvarado, M. J., Reid, J. S., Karl, T., Crouse, J. D., and Wennberg, P. O.:  
 838 Emission factors for open and domestic biomass burning for use in atmospheric models, Atmospheric Chem. Phys., 11,

839 4039–4072, <https://doi.org/10.5194/acp-11-4039-2011>, 2011.

840 Alexander, M. E. and Cruz, M. G.: Modelling the effects of surface and crown fire behaviour on serotinous cone opening in

841 jack pine and lodgepole pine forests, *Int. J. Wildland Fire*, 21, 709, <https://doi.org/10.1071/WF11153>, 2012.

842 Almendros, G. and González-Vila, F. J.: Wildfires, soil carbon balance and resilient organic matter in Mediterranean

843 ecosystems. A review ., *Span. J. Soil Sci.*, 2, 153, <https://doi.org/10.3232/SJSS.2012.V2.N2.01>, 2012.

844 Alonso-González, E. and Fernández-García, V.: MOSEV: a global burn severity database from MODIS (2000–2020), *Earth*

845 *Syst. Sci. Data*, 13, 1925–1938, <https://doi.org/10.5194/essd-13-1925-2021>, 2021.

846 Andela, N., Morton, D. C., Giglio, L., Paugam, R., Chen, Y., Hantson, S., Van Der Werf, G. R., and Randerson, J. T.: The

847 Global Fire Atlas of individual fire size, duration, speed and direction, *Earth Syst. Sci. Data*, 11, 529–552,

848 <https://doi.org/10.5194/essd-11-529-2019>, 2019.

849 Anon: Liste des bassins houillers français, Wikipédia, 2023.

850 BDIFF: <https://bdiff.agriculture.gouv.fr/>, last access: 8 March 2023.

851 CAMS | Copernicus: <https://atmosphere.copernicus.eu/global-fire-emissions>, last access: 22 September 2023.

852 Coal - Carbon, Organic Matter, Sedimentary Rock | Britannica: [https://www.britannica.com/science/coal-fossil-](https://www.britannica.com/science/coal-fossil-fuel/Structure-and-properties-of-coal)

853 [fuel/Structure-and-properties-of-coal](https://www.britannica.com/science/coal-fossil-fuel/Structure-and-properties-of-coal), last access: 25 July 2023.

854 GFAS:

855 <https://confluence.ecmwf.int/display/CKB/CAMS+global+biomass+burning+emissions+based+on+fire+radiative+power+%28GFAS%29%3A+data+documentation>, last access: 22 September 2023.

856 GFAS | Atmosphere Data Store: [https://ads.atmosphere.copernicus.eu/cdsapp#!/dataset/cams-global-fire-emissions-](https://ads.atmosphere.copernicus.eu/cdsapp#!/dataset/cams-global-fire-emissions-gfas?tab=overview)

857 [gfas?tab=overview](https://ads.atmosphere.copernicus.eu/cdsapp#!/dataset/cams-global-fire-emissions-gfas?tab=overview), last access: 22 September 2023.

858 ICOS: <https://www.icos-cp.eu/>, last access: 28 September 2023.

859 ICOS - FR: <https://icos-france.fr/en/>, last access: 28 September 2023.

860 IFN: <https://inventaire-forestier.ign.fr/>, last access: 9 October 2023a.

861 NASA-FIRMS: <https://firms.modaps.eosdis.nasa.gov/map/>, last access: 22 March 2023.

862 SIFA: <https://www.aeris-data.fr/projects/icos-service-national-dobservation-icos-france-atmosphere-sifa/>, last access: 18

863 October 2023.

864 apphim.fr - Les gisements de charbon et lignite: <https://apphim.fr/articles.php?lng=fr&pg=6343&mnuid=1136&tconfig=0>,

865 last access: 22 September 2023.

866 Artés, T., Oom, D., De Rigo, D., Durrant, T. H., Maianti, P., Libertà, G., and San-Miguel-Ayanz, J.: A global wildfire

867 dataset for the analysis of fire regimes and fire behaviour, *Sci. Data*, 6, 296, <https://doi.org/10.1038/s41597-019-0312-2>,

868 2019.

869 Asbjornsen, H., Velázquez-Rosas, N., García-Soriano, R., and Gallardo-Hernández, C.: Deep ground fires cause massive

870 above- and below-ground biomass losses in tropical montane cloud forests in Oaxaca, Mexico, *J. Trop. Ecol.*, 21, 427–434,

871 <https://doi.org/10.1017/S0266467405002373>, 2005.

872 Astiani, D., Curran, L., Burhanuddin, Taherzadeh, M., Mujiman, Hatta, M., Pamungkas, W., and Gusmayanti, E.: FIRE-

873 DRIVEN BIOMASS AND PEAT CARBON LOSSES AND POST-FIRE SOIL CO<sub>2</sub> EMISSION IN A WEST

874 KALIMANTAN PEATLAND FOREST, *J. Trop. For. Sci.*, 30, 570–575, <https://doi.org/10.26525/jtfs2018.30.4.570575>,

875 2018.

876 Atwood, E. C., Enghart, S., Lorenz, E., Halle, W., Wiedemann, W., and Siegert, F.: Detection and Characterization of Low

877 Temperature Peat Fires during the 2015 Fire Catastrophe in Indonesia Using a New High-Sensitivity Fire Monitoring

878 Satellite Sensor (FireBird), *PLOS ONE*, 11, e0159410, <https://doi.org/10.1371/journal.pone.0159410>, 2016.

879 Balde, B., Vega-Garcia, C., Gelabert, P. J., Ameztegui, A., and Rodrigues, M.: The relationship between fire severity and

880 burning efficiency for estimating wildfire emissions in Mediterranean forests, *J. For. Res.*, [https://doi.org/10.1007/s11676-](https://doi.org/10.1007/s11676-023-01599-1)

881 [023-01599-1](https://doi.org/10.1007/s11676-023-01599-1), 2023.

882 Bastarrika, A., Alvarado, M., Artano, K., Martinez, M., Mesanza, A., Torre, L., Ramo, R., and Chuvieco, E.: BAMS: A Tool

883 for Supervised Burned Area Mapping Using Landsat Data, *Remote Sens.*, 6, 12360–12380,

884 <https://doi.org/10.3390/rs61212360>, 2014.

885 Belgiu, M. and Drăguț, L.: Random forest in remote sensing: A review of applications and future directions, *ISPRS J.*

886 *Photogramm. Remote Sens.*, 114, 24–31, <https://doi.org/10.1016/j.isprsjprs.2016.01.011>, 2016.

887 Benali, A., Russo, A., Sá, A., Pinto, R., Price, O., Koutsias, N., and Pereira, J.: Determining Fire Dates and Locating Ignition

888

889 Points With Satellite Data, *Remote Sens.*, 8, 326, <https://doi.org/10.3390/rs8040326>, 2016.

890 Bertrand, G., Ponçot, A., Pohl, B., Lhosmot, A., Steinmann, M., Johannet, A., Pinel, S., Caldirak, H., Artigue, G., Binet, P.,  
891 Bertrand, C., Collin, L., Magnon, G., Gilbert, D., Laggoun-Defarge, F., and Toussaint, M.-L.: Statistical hydrology for  
892 evaluating peatland water table sensitivity to simple environmental variables and climate changes application to the mid-  
893 latitude/altitude Frasnian peatland (Jura Mountains, France), *Sci. Total Environ.*, 754, 141931,  
894 <https://doi.org/10.1016/j.scitotenv.2020.141931>, 2021.

895 Bourgeau-Chavez, L. L., Grelik, S. L., Billmire, M., Jenkins, L. K., Kasischke, E. S., and Turetsky, M. R.: Assessing Boreal  
896 Peat Fire Severity and Vulnerability of Peatlands to Early Season Wildland Fire, *Front. For. Glob. Change*, 3, 20,  
897 <https://doi.org/10.3389/ffgc.2020.00020>, 2020.

898 Brandt, M., Tucker, C. J., Kariryaa, A., Rasmussen, K., Abel, C., Small, J., Chave, J., Rasmussen, L. V., Hiernaux, P., Diouf,  
899 A. A., Kergoat, L., Mertz, O., Igel, C., Gieseke, F., Schöning, J., Li, S., Melocik, K., Meyer, J., Sinno, S., Romero, E.,  
900 Glennie, E., Montagu, A., Dendoncker, M., and Fensholt, R.: An unexpectedly large count of trees in the West African  
901 Sahara and Sahel, *Nature*, 587, 78–82, <https://doi.org/10.1038/s41586-020-2824-5>, 2020.

902 Breiman, L.: Random Forests, *Mach. Learn.*, 45, 5–32, <https://doi.org/10.1023/A:1010933404324>, 2001.

903 Brown, K.: Subterranean Coal Fires Spark Disaster, *Science*, 299, 1177–1177,  
904 <https://doi.org/10.1126/science.299.5610.1177b>, 2003.

905 Cardíl, A., Tapia, V. M., Monedero, S., Quñones, T., Little, K., Stoof, C. R., Ramirez, J., and de-Miguel, S.: Characterizing  
906 the rate of spread of large wildfires in emerging fire environments of northwestern Europe using Visible Infrared Imaging  
907 Radiometer Suite active fire data, *Nat. Hazards Earth Syst. Sci.*, 23, 361–373, <https://doi.org/10.5194/nhess-23-361-2023>,  
908 2023.

909 Carter, T. S., Heald, C. L., Jimenez, J. L., Campuzano-Jost, P., Kondo, Y., Moteki, N., Schwarz, J. P., Wiedinmyer, C.,  
910 Darmenov, A. S., Da Silva, A. M., and Kaiser, J. W.: How emissions uncertainty influences the distribution and radiative  
911 impacts of smoke from fires in North America, *Atmospheric Chem. Phys.*, 20, 2073–2097, <https://doi.org/10.5194/acp-20-2073-2020>, 2020.

913 Certini, G., Nocentini, C., Knicker, H., Arfaio, P., and Rumpel, C.: Wildfire effects on soil organic matter quantity and  
914 quality in two fire-prone Mediterranean pine forests, *Geoderma*, 167–168, 148–155,  
915 <https://doi.org/10.1016/j.geoderma.2011.09.005>, 2011.

916 Challa, V. S., Indranci, J., Baham, J. M., Patrick, C., Rabarison, M. K., Young, J. H., Hughes, R., Swanier, S. J., Hardy, M.  
917 G., and Yerramilli, A.: Sensitivity of atmospheric dispersion simulations by HYSPLIT to the meteorological predictions  
918 from a meso-scale model, *Environ. Fluid Mech.*, 8, 367–387, <https://doi.org/10.1007/s10652-008-9098-z>, 2008.

919 Chen, Y., Hantson, S., Andela, N., Coffield, S. R., Graff, C. A., Morton, D. C., Ott, L. E., Fofoula-Georgiou, E., Smyth, P.,  
920 Goulden, M. L., and Randerson, J. T.: California wildfire spread derived using VIIRS satellite observations and an object-  
921 based tracking system, *Sci. Data*, 9, 249, <https://doi.org/10.1038/s41597-022-01343-0>, 2022.

922 Chuvieco, E., Mouillot, F., Van Der Werf, G. R., San Miguel, J., Tanase, M., Koutsias, N., García, M., Yebra, M., Padilla,  
923 M., Gitas, I., Heil, A., Hawbaker, T. J., and Giglio, L.: Historical background and current developments for mapping burned  
924 area from satellite Earth observation, *Remote Sens. Environ.*, 225, 45–64, <https://doi.org/10.1016/j.rse.2019.02.013>, 2019.

925 Chuvieco, E., Roteta, E., Sali, M., Stroppiana, D., Boettcher, M., Kirches, G., Storm, T., Khairoun, A., Pettinari, M. L.,  
926 Franquesa, M., and Albergel, C.: Building a small fire database for Sub-Saharan Africa from Sentinel-2 high-resolution  
927 images, *Sci. Total Environ.*, 845, 157139, <https://doi.org/10.1016/j.scitotenv.2022.157139>, 2022.

928 Chuvieco, E., Yebra, M., Martino, S., Thonicke, K., Gómez-Giménez, M., San-Miguel, J., Oom, D., Velea, R., Mouillot, F.,  
929 Molina, J. R., Miranda, A. I., Lopes, D., Salis, M., Bugaric, M., Sofiev, M., Kadantsev, E., Gitas, I. Z., Stavrakoudis, D.,  
930 Eftychidis, G., Bar-Massada, A., Neidermeier, A., Pampanoni, V., Pettinari, M. L., Arrogante-Funes, F., Ochoa, C., Moreira,  
931 B., and Viegas, D.: Towards an Integrated Approach to Wildfire Risk Assessment: When, Where, What and How May the  
932 Landscapes Burn, *Fire*, 6, 215, <https://doi.org/10.3390/fire6050215>, 2023.

933 Citepa: Gaz à effet de serre et polluants atmosphériques. Bilan des émissions en France de 1990 à 2022. Rapport Secten,  
934 2023.

935 Cobian-Iñiguez, J., Richter, F., Carmignani, L., Liveretou, C., Xiong, H., Stephens, S., Finney, M., Gollner, M., and  
936 Fernandez-Pello, C.: Wind Effects on Smoldering Behavior of Simulated Wildland Fuels, *Combust. Sci. Technol.*, 1–18,  
937 <https://doi.org/10.1080/00102202.2021.2019239>, 2022.

938 Conil, S., Helle, J., Langrene, L., Laurent, O., Delmotte, M., and Ramonet, M.: Continuous atmospheric

939 CO<sub>2</sub>, CH<sub>4</sub>; and CO measurements at the Observatoire Pérenne de  
940 l'Environnement (OPE) station in France from 2011 to 2018, *Atmospheric Meas. Tech.*, 12, 6361–6383,  
941 <https://doi.org/10.5194/amt-12-6361-2019>, 2019.

942 CORINE Land Cover 2018: <https://land.copernicus.eu/pan-european/corine-land-cover/clc2018>, last access: 2 February  
943 2023.

944 Cornelissen, J. H. C., Sibma, F., Van Logtestijn, R. S. P., Broekman, R. A., and Thompson, K.: Leaf pH as a plant trait:  
945 species-driven rather than soil-driven variation: Species versus soil chemistry effects on leaf pH, *Funct. Ecol.*, 25, 449–455,  
946 <https://doi.org/10.1111/j.1365-2435.2010.01765.x>, 2011.

947 Cruz, M. G., Alexander, M. E., and Kilinc, M.: Wildfire Rates of Spread in Grasslands under Critical Burning Conditions,  
948 *Fire*, 5, 55, <https://doi.org/10.3390/fire5020055>, 2022.

949 Davies, G. M., Gray, A., Rein, G., and Legg, C. J.: Peat consumption and carbon loss due to smouldering wildfire in a  
950 temperate peatland, *For. Ecol. Manag.*, 308, 169–177, <https://doi.org/10.1016/j.foreco.2013.07.051>, 2013.

951 De Vos, B., Cools, N., Ilvesniemi, H., Vesterdal, L., Vanguelova, E., and Carnicelli, S.: Benchmark values for forest soil  
952 carbon stocks in Europe: Results from a large scale forest soil survey, *Geoderma*, 251–252, 33–46,  
953 <https://doi.org/10.1016/j.geoderma.2015.03.008>, 2015.

954 Desservettaz, M. J., Fisher, J. A., Luhar, A. K., Woodhouse, M. T., Bukosa, B., Buchholz, R. R., Wiedinmyer, C., Griffith,  
955 D. W. T., Krummel, P. B., Jones, N. B., Deutscher, N. M., and Greenslade, J. W.: Australian Fire Emissions of Carbon  
956 Monoxide Estimated by Global Biomass Burning Inventories: Variability and Observational Constraints, *J. Geophys. Res.*  
957 *Atmospheres*, 127, <https://doi.org/10.1029/2021JD035925>, 2022.

958 East, A., Hansen, A., Armenteras, D., Jantz, P., and Roberts, D. W.: Measuring Understory Fire Effects from Space: Canopy  
959 Change in Response to Tropical Understory Fire and What This Means for Applications of GEDI to Tropical Forest Fire,  
960 *Remote Sens.*, 15, 696, <https://doi.org/10.3390/rs15030696>, 2023.

961 European Commission. Joint Research Centre.: Advance report on forest fires in Europe, Middle East and North Africa  
962 2022., Publications Office, LU, 2023.

963 Fernández-Guisuraga, J. M., Calvo, L., Fernandes, P. M., and Suárez-Seoane, S.: Short-Term Recovery of the Aboveground  
964 Carbon Stock in Iberian Shrublands at the Extremes of an Environmental Gradient and as a Function of Burn Severity,  
965 *Forests*, 13, 145, <https://doi.org/10.3390/f13020145>, 2022.

966 Fisher, D., Wooster, M. J., Xu, W., Thomas, G., and Lestari, P.: Top-Down Estimation of Particulate Matter Emissions from  
967 Extreme Tropical Peatland Fires Using Geostationary Satellite Fire Radiative Power Observations, *Sensors*, 20, 7075,  
968 <https://doi.org/10.3390/s20247075>, 2020.

969 Franquesa, M., Vanderhoof, M. K., Stavrakoudis, D., Gitas, I. Z., Roteta, E., Padilla, M., and Chuvieco, E.: Development of  
970 a standard database of reference sites for validating global burned area products, *Earth Syst. Sci. Data*, 12, 3229–3246,  
971 <https://doi.org/10.5194/essd-12-3229-2020>, 2020.

972 Fredriksson, G.: Extinguishing the 1998 forest fires and subsequent coal fires in the Sungai Wain Protection Forest , East  
973 Kalimantan , Indonesia, Citation Key: Fredriksson2004ExtinguishingT1, 2004.

974 Freeborn, P. H., Wooster, M. J., Roy, D. P., and Cochrane, M. A.: Quantification of MODIS fire radiative power (FRP)  
975 measurement uncertainty for use in satellite-based active fire characterization and biomass burning estimation, *Geophys.*  
976 *Res. Lett.*, 41, 1988–1994, <https://doi.org/10.1002/2013GL059086>, 2014.

977 Galizia, L. F., Barbero, R., Rodrigues, M., Ruffault, J., Pimont, F., and Curt, T.: Global Warming Reshapes European  
978 Pyroregions, *Earths Future*, 11, e2022EF003182, <https://doi.org/10.1029/2022EF003182>, 2023.

979 García, M. J. L. and Caselles, V.: Mapping burns and natural reforestation using thematic Mapper data, *Geocarto Int.*, 6, 31–  
980 37, <https://doi.org/10.1080/10106049109354290>, 1991.

981 Garcia-Hurtado, E., Pey, J., Baeza, M. J., Carrara, A., Llovet, J., Querol, X., Alastuey, A., and Vallejo, V. R.: Carbon  
982 emissions in Mediterranean shrubland wildfires: An experimental approach, *Atmos. Environ.*, 69, 86–93,  
983 <https://doi.org/10.1016/j.atmosenv.2012.11.063>, 2013.

984 Garlough, E. C. and Keyes, C. R.: Influences of moisture content, mineral content and bulk density on smouldering  
985 combustion of ponderosa pine duff mounds, *Int. J. Wildland Fire*, 20, 589, <https://doi.org/10.1071/WF10048>, 2011.

986 Le lignite d'Hostens: <http://www.geocaching.com/>, last access: 25 July 2023.

987 Geron, C. and Hays, M.: Air emissions from organic soil burning on the coastal plain of North Carolina, *Atmos. Environ.*,  
988 64, 192–199, <https://doi.org/10.1016/j.atmosenv.2012.09.065>, 2013.

989 Gerrand, S., Aspinall, J., Jensen, T., Hopkinson, C., Collingwood, A., and Chasmer, L.: Partitioning carbon losses from fire  
990 combustion in a montane Valley, Alberta Canada, *For. Ecol. Manag.*, 496, 119435,  
991 <https://doi.org/10.1016/j.foreco.2021.119435>, 2021.

992 Giglio, Louis: MODIS Thermal Anomalies/Fire Products, <https://doi.org/10.5067/FIRMS/MODIS/MCD14ML>, 2000.

993 Giglio, L., Schroeder, W., and Justice, C. O.: The collection 6 MODIS active fire detection algorithm and fire products,  
994 *Remote Sens. Environ.*, 178, 31–41, <https://doi.org/10.1016/j.rse.2016.02.054>, 2016.

995 Gogo, S., Paroissien, J., Laggoun-Défarge, F., Antoine, J., Bernard-Jannin, L., Bertrand, G., Binet, P., Binet, S., Bouger, G.,  
996 Brossard, Y., Camboulive, T., Caudal, J., Chevrier, S., Chiapiuso, G., D’Angelo, B., Durantez, P., Flechard, C., Francez, A.,  
997 Galop, D., Gandois, L., Gilbert, D., Guimbaud, C., Hinault, L., Jacotot, A., Le Moing, F., Lerigoleur, E., Le Roux, G., Leroy,  
998 F., Lhosmot, A., Li, Q., Machado Da Silva, E., Moquet, J., Mora-Gomez, J., Perdereau, L., Rosset, T., and Toussaint, M.:  
999 The information system of the French Peatland Observation Service: Service National d’Observation Tourbières – A  
1000 valuable tool to assess the impact of global changes on the hydrology and biogeochemistry of temperate peatlands through  
1001 long term monitoring, *Hydrol. Process.*, 35, <https://doi.org/10.1002/hyp.14244>, 2021.

1002 Graham, L. L. B., Applegate, G. B., Thomas, A., Ryan, K. C., Saharjo, B. H., and Cochrane, M. A.: A Field Study of  
1003 Tropical Peat Fire Behaviour and Associated Carbon Emissions, *Fire*, 5, 62, <https://doi.org/10.3390/fire5030062>, 2022.

1004 Gräler, B., Pebesma, E., and Heuvelink, G.: Spatio-Temporal Interpolation using gstat, *R J.*, 8, 204–218, 2016.

1005 Griffin, D., Chen, J., Anderson, K., Makar, P., McLinden, C. A., Dammers, E., and Fogal, A.: Towards an improved  
1006 understanding of wildfire CO emissions: a satellite remote-sensing perspective, *Gases/Remote Sensing/Troposphere/Physics*  
1007 (physical properties and processes), <https://doi.org/10.5194/egusphere-2023-649>, 2023.

1008 Hall, J. V., Zibtsev, S. V., Giglio, L., Skakun, S., Myroniuk, V., Zhuravel, O., Goldammer, J. G., and Kussul, N.:  
1009 Environmental and political implications of underestimated cropland burning in Ukraine, *Environ. Res. Lett.*, 16, 064019,  
1010 <https://doi.org/10.1088/1748-9326/abfc04>, 2021.

1011 Hantson, S., Andela, N., Goulden, M. L., and Randerson, J. T.: Human-ignited fires result in more extreme fire behavior and  
1012 ecosystem impacts, *Nat. Commun.*, 13, 2717, <https://doi.org/10.1038/s41467-022-30030-2>, 2022.

1013 Hao, W. M. and Ward, D. E.: Methane production from global biomass burning, *J. Geophys. Res. Atmospheres*, 98, 20657–  
1014 20661, <https://doi.org/10.1029/93JD01908>, 1993.

1015 Heiskanen, J., Brümmer, C., Buchmann, N., Calfapietra, C., Chen, H., Gielen, B., Gkritzalis, T., Hammer, S., Hartman, S.,  
1016 Herbst, M., Janssens, I. A., Jordan, A., Juurola, E., Karstens, U., Kasurinen, V., Kruijt, B., Lankreijer, H., Levin, I.,  
1017 Linderson, M.-L., Loustau, D., Merbold, L., Myhre, C. L., Papale, D., Pavelka, M., Pilegaard, K., Ramonet, M., Rebmann,  
1018 C., Rinne, J., Rivier, L., Saltikoff, E., Sanders, R., Steinbacher, M., Steinhoff, T., Watson, A., Vermeulen, A. T., Vesala, T.,  
1019 Vítková, G., and Kutsch, W.: The Integrated Carbon Observation System in Europe, *Bull. Am. Meteorol. Soc.*, 103, E855–  
1020 E872, <https://doi.org/10.1175/BAMS-D-19-0364.1>, 2022.

1021 Hersbach, H., Bell, B., Berrisford, P., Hirahara, S., Horányi, A., Muñoz-Sabater, J., Nicolas, J., Peubey, C., Radu, R.,  
1022 Schepers, D., Simmons, A., Soci, C., Abdalla, S., Abellan, X., Balsamo, G., Bechtold, P., Biavati, G., Bidlot, J., Bonavita,  
1023 M., De Chiara, G., Dahlgren, P., Dee, D., Diamantakis, M., Dragani, R., Flemming, J., Forbes, R., Fuentes, M., Geer, A.,  
1024 Haimberger, L., Healy, S., Hogan, R. J., Hólm, E., Janisková, M., Keeley, S., Laloyaux, P., Lopez, P., Lupu, C., Radnoti, G.,  
1025 De Rosnay, P., Rozum, I., Vamborg, F., Villaume, S., and Thépaut, J.: The ERA5 global reanalysis, *Q. J. R. Meteorol. Soc.*,  
1026 146, 1999–2049, <https://doi.org/10.1002/qj.3803>, 2020.

1027 Hille, M. and Den Ouden, J.: Fuel load, humus consumption and humus moisture dynamics in Central European Scots pine  
1028 stands, *Int. J. Wildland Fire*, 14, 153, <https://doi.org/10.1071/WF04026>, 2005.

1029 Hu, Y. and Rein, G.: Development of gas signatures of smouldering peat wildfire from emission factors, *Int. J. Wildland*  
1030 *Fire*, 31, 1014–1032, <https://doi.org/10.1071/WF21093>, 2022.

1031 Hu, Y., Christensen, E., Restuccia, F., and Rein, G.: Transient gas and particle emissions from smouldering combustion of  
1032 peat, *Proc. Combust. Inst.*, 37, 4035–4042, <https://doi.org/10.1016/j.proci.2018.06.008>, 2019.

1033 Huang, X. and Rein, G.: Downward spread of smouldering peat fire: the role of moisture, density and oxygen supply, *Int. J.*  
1034 *Wildland Fire*, 26, 907, <https://doi.org/10.1071/WF16198>, 2017.

1035 IFN: <https://inventaire-forestier.ign.fr/spip.php?article773>, last access: 9 March 2023b.

1036 Irannezhad, M., Liu, J., Ahmadi, B., and Chen, D.: The dangers of Arctic zombie wildfires, *Science*, 369, 1171–1171,  
1037 <https://doi.org/10.1126/science.abe1739>, 2020.

1038 Johnston, J., Johnston, L., Wooster, M., Brookes, A., McFayden, C., and Cantin, A.: Satellite Detection Limitations of Sub-

1039 Canopy Smouldering Wildfires in the North American Boreal Forest, *Fire*, 1, 28, <https://doi.org/10.3390/fire1020028>, 2018.

1040 Jonard, M., Nicolas, M., Coomes, D. A., Caignet, I., Saenger, A., and Ponette, Q.: Forest soils in France are sequestering

1041 substantial amounts of carbon, *Sci. Total Environ.*, 574, 616–628, <https://doi.org/10.1016/j.scitotenv.2016.09.028>, 2017.

1042 Kaiser, J. W., Heil, A., Andreae, M. O., Benedetti, A., Chubarova, N., Jones, L., Morcrette, J.-J., Razinger, M., Schultz, M.

1043 G., Suttie, M., and Van Der Werf, G. R.: Biomass burning emissions estimated with a global fire assimilation system based

1044 on observed fire radiative power, *Biogeosciences*, 9, 527–554, <https://doi.org/10.5194/bg-9-527-2012>, 2012.

1045 Key, C. H. and Benson, N. C.: The normalized burn ratio (NBR): A landsat TM radiometric measure of burn severity, *U. S.*

1046 *Geol. Surv. North. Rocky Mt. Sci. Cent. Bozeman MT USA*, 1999.

1047 Kirkland, M., Atkinson, P. W., Pearce-Higgins, J. W., De Jong, M. C., Dowling, T. P. F., Grummo, D., Critchley, M., and

1048 Ashton-Butt, A.: Landscape fires disproportionately affect high conservation value temperate peatlands, meadows, and

1049 deciduous forests, but only under low moisture conditions, *Sci. Total Environ.*, 884, 163849,

1050 <https://doi.org/10.1016/j.scitotenv.2023.163849>, 2023.

1051 Kohlenberg, A. J., Turetsky, M. R., Thompson, D. K., Branfireun, B. A., and Mitchell, C. P. J.: Controls on boreal peat

1052 combustion and resulting emissions of carbon and mercury, *Environ. Res. Lett.*, 13, 035005, [https://doi.org/10.1088/1748-](https://doi.org/10.1088/1748-9326/aa9ea8)

1053 [9326/aa9ea8](https://doi.org/10.1088/1748-9326/aa9ea8), 2018.

1054 Kreye, J. K., Varner, J. M., Dugaw, C. J., Cao, J., Szecsei, J., and Engber, E. A.: Pine cones facilitate ignition of forest floor

1055 duff, *Can. J. For. Res.*, 43, 512–516, <https://doi.org/10.1139/cjfr-2013-0019>, 2013.

1056 Krishna, M. P. and Mohan, M.: Litter decomposition in forest ecosystems: a review, *Energy Ecol. Environ.*, 2, 236–249,

1057 <https://doi.org/10.1007/s40974-017-0064-9>, 2017.

1058 Kuklina, V., Sizov, O., Rasputina, E., Bilichenko, I., Krasnoshtanova, N., Bogdanov, V., and Petrov, A. N.: Fires on Ice:

1059 Emerging Permafrost Peatlands Fire Regimes in Russia’s Subarctic Taiga, *Land*, 11, 322,

1060 <https://doi.org/10.3390/land11030322>, 2022.

1061 Kurz-Besson, C., Coûteaux, M. M., Berg, B., Remacle, J., Ribeiro, C., Romanyà, J., and Thiéry, J. M.: A climate response

1062 function explaining most of the variation of the forest floor needle mass and the needle decomposition in pine forests across

1063 Europe, *Plant Soil*, 285, 97–114, <https://doi.org/10.1007/s11104-006-0061-9>, 2006.

1064 Laurent, P., Mouillot, F., Yue, C., Ciais, P., Moreno, M. V., and Nogueira, J. M. P.: FRY, a global database of fire patch

1065 functional traits derived from space-borne burned area products, *Sci. Data*, 5, 180132,

1066 <https://doi.org/10.1038/sdata.2018.132>, 2018.

1067 Laurent, P., Mouillot, F., Moreno, M. V., Yue, C., and Ciais, P.: Varying relationships between fire radiative power and fire

1068 size at a global scale, *Biogeosciences*, 16, 275–288, <https://doi.org/10.5194/bg-16-275-2019>, 2019.

1069 Lee, J. Y., Daube, C., Fortner, E., Ellsworth, N., May, N. W., Tallant, J., Herndon, S., and Pratt, K. A.: Chemical

1070 characterization of prescribed burn emissions from a mixed forest in Northern Michigan, *Environ. Sci. Atmospheres*, 3, 35–

1071 48, <https://doi.org/10.1039/D2EA00069E>, 2023.

1072 Lelandais, L., Xueref-Remy, I., Riandet, A., Blanc, P. E., Armengaud, A., Oppo, S., Yohia, C., Ramonet, M., and Delmotte,

1073 M.: Analysis of 5.5 years of atmospheric CO<sub>2</sub>, CH<sub>4</sub>, CO continuous observations (2014–2020) and their correlations, at the

1074 Observatoire de Haute Provence, a station of the ICOS-France national greenhouse gases observation network, *Atmos.*

1075 *Environ.*, 277, 119020, <https://doi.org/10.1016/j.atmosenv.2022.119020>, 2022.

1076 Lin, S., Liu, Y., and Huang, X.: How to build a firebreak to stop smouldering peat fire: insights from a laboratory-scale

1077 study, *Int. J. Wildland Fire*, 30, 454–461, <https://doi.org/10.1071/WF20155>, 2021.

1078 Lin, Z., Dai, Y., Mishra, U., Wang, G., Shangguan, W., Zhang, W., and Qin, Z.: On the magnitude and uncertainties of

1079 global and regional soil organic carbon: A comparative analysis using multiple estimates, *ESSD – Land/Pedology*,

1080 <https://doi.org/10.5194/essd-2022-232>, 2022.

1081 Lopez, M., Schmidt, M., Ramonet, M., Bonne, J.-L., Colomb, A., Kazan, V., Laj, P., and Pichon, J.-M.: Three years of

1082 semicontinuous greenhouse gas measurements at the Puy de Dôme station (central France), *Atmospheric Meas. Tech.*, 8,

1083 3941–3958, <https://doi.org/10.5194/amt-8-3941-2015>, 2015.

1084 Loustau, D.: *Forests, carbon cycle and climate change*, Éd. Quae, Versailles, 2010.

1085 Mack, M. C., Walker, X. J., Johnstone, J. F., Alexander, H. D., Melvin, A. M., Jean, M., and Miller, S. N.: Carbon loss from

1086 boreal forest wildfires offset by increased dominance of deciduous trees, *Science*, 372, 280–283,

1087 <https://doi.org/10.1126/science.abf3903>, 2021.

1088 Madrigal, J., Hernando, C., Guijarro, M., Vega, J. A., Fontúrbel, T., and Pérez-Gorostiaga, P.: Smouldering fire-induced

1089 changes in a Mediterranean soil (SE Spain): effects on germination, survival and morphological traits of 3-year-old *Pinus*  
1090 *pinaster* Ait., *Plant Ecol.*, 208, 279–292, <https://doi.org/10.1007/s11258-009-9705-1>, 2010.

1091 Magro, C., Nunes, L., Gonçalves, O., Neng, N., Nogueira, J., Rego, F., and Vieira, P.: Atmospheric Trends of CO and CH<sub>4</sub>  
1092 from Extreme Wildfires in Portugal Using Sentinel-5P TROPOMI Level-2 Data, *Fire*, 4, 25,  
1093 <https://doi.org/10.3390/fire4020025>, 2021.

1094 Majdalani, G., Koutsias, N., Faour, G., Adjizian-Gerard, J., and Mouillot, F.: Fire Regime Analysis in Lebanon (2001–  
1095 2020): Combining Remote Sensing Data in a Scarcely Documented Area, *Fire*, 5, 141, <https://doi.org/10.3390/fire5050141>,  
1096 2022.

1097 Martin, M., Saby, N., Toutain, B., Chenu, J.-P., Ratié, C., and Bouillon, L.: carbonStocksRegLu.csv,  
1098 <https://doi.org/10.15454/RURZXN/91UG74>, 2019.

1099 Masuda, C., Kanno, H., Masaka, K., Morikawa, Y., Suzuki, M., Tada, C., Hayashi, S., and Seiwa, K.: Hardwood mixtures  
1100 facilitate leaf litter decomposition and soil nitrogen mineralization in conifer plantations, *For. Ecol. Manag.*, 507, 120006,  
1101 <https://doi.org/10.1016/j.foreco.2021.120006>, 2022.

1102 McCarty, J. L., Aalto, J., Paunu, V.-V., Arnold, S. R., Eckhardt, S., Klimont, Z., Fain, J. J., Evangelidou, N., Venäläinen, A.,  
1103 Tchebakova, N. M., Parfenova, E. I., Kupiainen, K., Soja, A. J., Huang, L., and Wilson, S.: Reviews and syntheses: Arctic  
1104 fire regimes and emissions in the 21st century, *Biogeosciences*, 18, 5053–5083, <https://doi.org/10.5194/bg-18-5053-2021>,  
1105 2021.

1106 Mebust, A. K., Russell, A. R., Hudman, R. C., Valin, L. C., and Cohen, R. C.: Characterization of wildfire  
1107 NO<sub>x</sub> emissions using MODIS fire radiative power and OMI tropospheric  
1108 NO<sub>2</sub> columns, *Atmospheric Chem. Phys.*, 11, 5839–5851, [https://doi.org/10.5194/acp-11-5839-](https://doi.org/10.5194/acp-11-5839-2011)  
1109 2011, 2011.

1110 Mekonnen, Z. A., Riley, W. J., Randerson, J. T., Shirley, I. A., Bouskill, N. J., and Grant, R. F.: Wildfire exacerbates high-  
1111 latitude soil carbon losses from climate warming, *Environ. Res. Lett.*, 17, 094037, [https://doi.org/10.1088/1748-](https://doi.org/10.1088/1748-9326/ac8be6)  
1112 9326/ac8be6, 2022.

1113 Menut, L., Cholakian, A., Siour, G., Lapere, R., Pennel, R., Mailler, S., and Bessagnet, B.: Impact of Landes forest fires on  
1114 air quality in France during the summer 2022, *Aerosols/Atmospheric Modelling and Data Analysis/Troposphere/Chemistry*  
1115 (chemical composition and reactions), <https://doi.org/10.5194/egusphere-2023-421>, 2023.

1116 Mickler, R. A., Welch, D. P., and Bailey, A. D.: Carbon Emissions during Wildland Fire on a North American Temperate  
1117 Peatland, *Fire Ecol.*, 13, 34–57, <https://doi.org/10.4996/fireecology.1301034>, 2017.

1118 Miyaniishi, K. and Johnson, E. A.: Process and patterns of duff consumption in the mixedwood boreal forest, *Can. J. For.*  
1119 *Res.*, 32, 1285–1295, <https://doi.org/10.1139/x02-051>, 2002.

1120 Moreno-Martínez, Á., Camps-Valls, G., Kattge, J., Robinson, N., Reichstein, M., Van Bodegom, P., Kramer, K.,  
1121 Cornelissen, J. H. C., Reich, P., Bahn, M., Niinemets, Ü., Peñuelas, J., Craine, J. M., Cerabolini, B. E. L., Míndez, V.,  
1122 Laughlin, D. C., Sack, L., Allred, B., Baraloto, C., Byun, C., Soudzilovskaia, N. A., and Running, S. W.: A methodology to  
1123 derive global maps of leaf traits using remote sensing and climate data, *Remote Sens. Environ.*, 218, 69–88,  
1124 <https://doi.org/10.1016/j.rse.2018.09.006>, 2018.

1125 Mota, B. and Wooster, M. J.: A new top-down approach for directly estimating biomass burning emissions and fuel  
1126 consumption rates and totals from geostationary satellite fire radiative power (FRP), *Remote Sens. Environ.*, 206, 45–62,  
1127 <https://doi.org/10.1016/j.rse.2017.12.016>, 2018.

1128 Mouillot, F., Schultz, M. G., Yue, C., Cadule, P., Tansey, K., Ciais, P., and Chuvieco, E.: Ten years of global burned area  
1129 products from spaceborne remote sensing—A review: Analysis of user needs and recommendations for future developments,  
1130 *Int. J. Appl. Earth Obs. Geoinformation*, 26, 64–79, <https://doi.org/10.1016/j.jag.2013.05.014>, 2014.

1131 Muller, F.: Strategies for peatland conservation in France - a review of progress, *Mires Peat*, 1–13,  
1132 <https://doi.org/10.19189/MaP.2016.OMB.218>, 2018.

1133 National Centers For Environmental Prediction/National Weather Service/NOAA/U.S. Department Of Commerce: NCEP  
1134 GFS 0.25 Degree Global Forecast Grids Historical Archive, <https://doi.org/10.5065/D65D8PWK>, 2015.

1135 Parks, S. A.: Mapping day-of-burning with coarse-resolution satellite fire-detection data, *Int. J. Wildland Fire*, 23, 215,  
1136 <https://doi.org/10.1071/WF13138>, 2014.

1137 Pilloix, M.: Inventaire des tourbières françaises et du stock de carbone qu’elles contiennent, 2019.

1138 Prat-Guitart, N., Rein, G., Hadden, R. M., Belcher, C. M., and Yearsley, J. M.: Propagation probability and spread rates of



1139 self-sustained smouldering fires under controlled moisture content and bulk density conditions, *Int. J. Wildland Fire*, 25, 456,  
1140 <https://doi.org/10.1071/WF15103>, 2016.

1141 Pribyl, D. W.: A critical review of the conventional SOC to SOM conversion factor, *Geoderma*, 156, 75–83,  
1142 <https://doi.org/10.1016/j.geoderma.2010.02.003>, 2010.

1143 Prichard, S. J., O’Neill, S. M., Eagle, P., Andreu, A. G., Drye, B., Dubowy, J., Urbanski, S., and Strand, T. M.: Wildland fire  
1144 emission factors in North America: synthesis of existing data, measurement needs and management applications, *Int. J.*  
1145 *Wildland Fire*, 29, 132, <https://doi.org/10.1071/WF19066>, 2020.

1146 Ramonet, M., Ciais, P., Apadula, F., Bartyzel, J., Bastos, A., Bergamaschi, P., Blanc, P. E., Brunner, D., Caracciolo Di  
1147 Torchiarolo, L., Calzolari, F., Chen, H., Chmura, L., Colomb, A., Conil, S., Cristofanelli, P., Cuevas, E., Curcoll, R.,  
1148 Delmotte, M., Di Sarra, A., Emmenegger, L., Forster, G., Frumau, A., Gerbig, C., Gheusi, F., Hammer, S., Haszpra, L.,  
1149 Hatakka, J., Hazan, L., Heliasz, M., Henne, S., Hensen, A., Hermansen, O., Keronen, P., Kivi, R., Komínková, K., Kubistin,  
1150 D., Laurent, O., Laurila, T., Lavric, J. V., Lehner, I., Lehtinen, K. E. J., Leskinen, A., Leuenberger, M., Levin, I., Lindauer,  
1151 M., Lopez, M., Myhre, C. L., Mammarella, I., Manca, G., Manning, A., Marek, M. V., Marklund, P., Martin, D., Meinhardt,  
1152 F., Mihalopoulos, N., Mölder, M., Morgui, J. A., Necki, J., O’Doherty, S., O’Dowd, C., Ottosson, M., Philippon, C.,  
1153 Piacentino, S., Pichon, J. M., Plass-Duelmer, C., Resovsky, A., Rivier, L., Rodó, X., Sha, M. K., Scheeren, H. A., Sferlazzo,  
1154 D., Spain, T. G., Stanley, K. M., Steinbacher, M., Trisolino, P., Vermeulen, A., Vítková, G., Weyrauch, D., Xueref-Remy, I.,  
1155 Yala, K., and Yver Kwok, C.: The fingerprint of the summer 2018 drought in Europe on ground-based atmospheric CO<sub>2</sub>  
1156 measurements, *Philos. Trans. R. Soc. B Biol. Sci.*, 375, 20190513, <https://doi.org/10.1098/rstb.2019.0513>, 2020.

1157 Reddy, A. D., Hawbaker, T. J., Wurster, F., Zhu, Z., Ward, S., Newcomb, D., and Murray, R.: Quantifying soil carbon loss  
1158 and uncertainty from a peatland wildfire using multi-temporal LiDAR, *Remote Sens. Environ.*, 170, 306–316,  
1159 <https://doi.org/10.1016/j.rse.2015.09.017>, 2015.

1160 Rein, G., Cohen, S., and Simeoni, A.: Carbon emissions from smouldering peat in shallow and strong fronts, *Proc. Combust.*  
1161 *Inst.*, 32, 2489–2496, <https://doi.org/10.1016/j.proci.2008.07.008>, 2009.

1162 Rodrigues, M., Cunill Camprubí, À., Balaguer-Romano, R., Coco Megía, C. J., Castañares, F., Ruffault, J., Fernandes, P. M.,  
1163 and Resco de Dios, V.: Drivers and implications of the extreme 2022 wildfire season in Southwest Europe, *Sci. Total*  
1164 *Environ.*, 859, 160320, <https://doi.org/10.1016/j.scitotenv.2022.160320>, 2023.

1165 Roteta, E., Bastarrika, A., Franquesa, M., and Chuvieco, E.: Landsat and Sentinel-2 Based Burned Area Mapping Tools in  
1166 Google Earth Engine, *Remote Sens.*, 13, 816, <https://doi.org/10.3390/rs13040816>, 2021.

1167 Rouse, J. W., Haas, R. H., Deering, D. W., Schell, J. A., and Harlan, J. C.: Monitoring the Vernal Advancement and  
1168 Retrogradation (Green Wave Effect) of Natural Vegetation, 1974.

1169 Roy, D. P., Boschetti, L., and Trigg, S. N.: Remote Sensing of Fire Severity: Assessing the Performance of the Normalized  
1170 Burn Ratio, *IEEE Geosci. Remote Sens. Lett.*, 3, 112–116, <https://doi.org/10.1109/LGRS.2005.858485>, 2006.

1171 Ruffault, J. and Mouillot, F.: How a new fire-suppression policy can abruptly reshape the fire-weather relationship,  
1172 *Ecosphere*, 6, art199, <https://doi.org/10.1890/ES15-00182.1>, 2015.

1173 Ruffault, J., Curt, T., Moron, V., Trigo, R. M., Mouillot, F., Koutsias, N., Pimont, F., Martin-StPaul, N., Barbero, R., Dupuy,  
1174 J.-L., Russo, A., and Belhadj-Khedher, C.: Increased likelihood of heat-induced large wildfires in the Mediterranean Basin,  
1175 *Sci. Rep.*, 10, 13790, <https://doi.org/10.1038/s41598-020-70069-z>, 2020.

1176 Salis, M., Arca, B., Alcasena, F., Arianoutsou, M., Bacciu, V., Duce, P., Duguy, B., Koutsias, N., Mallinis, G., Mitsopoulos,  
1177 I., Moreno, J. M., Pérez, J. R., Urbieta, I. R., Xystrakis, F., Zavala, G., and Spano, D.: Predicting wildfire spread and  
1178 behaviour in Mediterranean landscapes, *Int. J. Wildland Fire*, 25, 1015, <https://doi.org/10.1071/WF15081>, 2016.

1179 Scaduto, E., Chen, B., and Jin, Y.: Satellite-Based Fire Progression Mapping: A Comprehensive Assessment for Large Fires  
1180 in Northern California, *IEEE J. Sel. Top. Appl. Earth Obs. Remote Sens.*, 13, 5102–5114,  
1181 <https://doi.org/10.1109/JSTARS.2020.3019261>, 2020.

1182 Schmidt, M., Lopez, M., Yver Kwok, C., Messenger, C., Ramonet, M., Wastine, B., Vuillemin, C., Truong, F., Gal, B.,  
1183 Parmentier, E., Cloué, O., and Ciais, P.: High-precision quasi-continuous atmospheric greenhouse gas measurements at  
1184 Trainou tower (Orléans forest, France), *Atmospheric Meas. Tech.*, 7, 2283–2296, <https://doi.org/10.5194/amt-7-2283-2014>,  
1185 2014.

1186 Scholten, R. C., Jandt, R., Miller, E. A., Rogers, B. M., and Veraverbeke, S.: Overwintering fires in boreal forests, *Nature*,  
1187 593, 399–404, <https://doi.org/10.1038/s41586-021-03437-y>, 2021.

1188 Schroeder, W., Oliva, P., Giglio, L., and Csiszar, I. A.: The New VIIRS 375 m active fire detection data product: Algorithm

1189 description and initial assessment, *Remote Sens. Environ.*, 143, 85–96, <https://doi.org/10.1016/j.rse.2013.12.008>, 2014.

1190 Schwartz, M., Ciais, P., De Truchis, A., Chave, J., Otlé, C., Vega, C., Wigneron, J.-P., Nicolas, M., Jouaber, S., Liu, S.,

1191 Brandt, M., and Fayad, I.: FORMS: Forest Multiple Source height, wood volume, and biomass maps in France at 10 to 30 m

1192 resolution based on Sentinel-1, Sentinel-2, and GEDI data with a deep learning approach, *ESSD – Land/Land Cover and*

1193 *Land Use*, <https://doi.org/10.5194/essd-2023-196>, 2023.

1194 SIFA: <https://www.aeris-data.fr/projects/icos-service-national-dobservation-icos-france-atmosphere-sifa/>, last access: 18

1195 October 2023.

1196 Sirin, A. and Medvedeva, M.: Remote Sensing Mapping of Peat-Fire-Burnt Areas: Identification among Other Wildfires,

1197 *Remote Sens.*, 14, 194, <https://doi.org/10.3390/rs14010194>, 2022.

1198 Song, Z., Huang, X., Jiang, J., and Pan, X.: A laboratory approach to CO<sub>2</sub> and CO emission factors from underground coal

1199 fires, *Int. J. Coal Geol.*, 219, 103382, <https://doi.org/10.1016/j.coal.2019.103382>, 2020.

1200 Soukissian, T. and Sotiriou, M.-A.: Long-Term Variability of Wind Speed and Direction in the Mediterranean Basin, *Wind*,

1201 2, 513–534, <https://doi.org/10.3390/wind2030028>, 2022.

1202 Stein, A. F., Draxler, R. R., Rolph, G. D., Stunder, B. J. B., Cohen, M. D., and Ngan, F.: NOAA’s HYSPLIT Atmospheric

1203 Transport and Dispersion Modeling System, *Bull. Am. Meteorol. Soc.*, 96, 2059–2077, [https://doi.org/10.1175/BAMS-D-14-](https://doi.org/10.1175/BAMS-D-14-00110.1)

1204 00110.1, 2015.

1205 Stracher, G. B. and Taylor, T. P.: Coal fires burning out of control around the world: thermodynamic recipe for

1206 environmental catastrophe, *Int. J. Coal Geol.*, 59, 7–17, <https://doi.org/10.1016/j.coal.2003.03.002>, 2004.

1207 Ouest-France: Feux « zombies » à l’origine de la reprise des incendies en Gironde : on vous explique ce phénomène, *Ouest-*

1208 *Francefr*, 2022.

1209 Tang, S., Yin, S., Shan, Y., Yu, B., Cui, C., and Cao, L.: The Characteristics of Gas and Particulate Emissions from

1210 Smouldering Combustion in the *Pinus pumila* Forest of Huzhong National Nature Reserve of the Daxing’an Mountains,

1211 *Forests*, 14, 364, <https://doi.org/10.3390/f14020364>, 2023.

1212 Tanneberger, F., Tegetmeyer, C., Busse, S., Barthelmes, A., and 55 others: The peatland map of Europe, *Mires Peat*, 1–

1213 17, <https://doi.org/10.19189/MaP.2016.OMB.264>, 2017.

1214 Tukey, J. W.: *Exploratory data analysis*, Vol. 2, pp. 131–160, 1977.

1215 Turetsky, M. R., Donahue, W. F., and Benscoter, B. W.: Experimental drying intensifies burning and carbon losses in a

1216 northern peatland, *Nat. Commun.*, 2, 514, <https://doi.org/10.1038/ncomms1523>, 2011a.

1217 Turetsky, M. R., Kane, E. S., Harden, J. W., Ottmar, R. D., Manies, K. L., Hoy, E., and Kasischke, E. S.: Recent acceleration

1218 of biomass burning and carbon losses in Alaskan forests and peatlands, *Nat. Geosci.*, 4, 27–31,

1219 <https://doi.org/10.1038/ngeo1027>, 2011b.

1220 Usman, M., Sitanggang, I. S., and Syaufina, L.: Hotspot Distribution Analyses Based on Peat Characteristics Using Density-

1221 based Spatial Clustering, *Procedia Environ. Sci.*, 24, 132–140, <https://doi.org/10.1016/j.proenv.2015.03.018>, 2015.

1222 Vallet, L., Schwartz, M., Ciais, P., Van Wees, D., De Truchis, A., and Mouillot, F.: High-resolution data reveal a surge of

1223 biomass loss from temperate and Atlantic pine forests, contextualizing the 2022 fire season distinctiveness in France,

1224 *Biogeosciences*, 20, 3803–3825, <https://doi.org/10.5194/bg-20-3803-2023>, 2023.

1225 Vallet, L., Ciais, P., van Wees, D., de Truchis, A., and Mouillot, F.: Forest biomass loss by fire 2020–2022 in France,

1226 <https://doi.org/10.15148/3DB37FDF-46B1-4E7A-BD86-CA4FB93307E1>, 2023.

1227 Van Der Velde, I. R., Van Der Werf, G. R., Houweling, S., Eskes, H. J., Veeffkind, J. P., Borsdorff, T., and Aben, I.:

1228 Biomass burning combustion efficiency observed from space using measurements of CO and NO<sub>2</sub> by the TROPospheric Monitoring Instrument (TROPOMI), *Atmospheric Chem. Phys.*, 21, 597–616,

1229 <https://doi.org/10.5194/acp-21-597-2021>, 2021.

1230

1231 Van Der Werf, G. R., Randerson, J. T., Giglio, L., Van Leeuwen, T. T., Chen, Y., Rogers, B. M., Mu, M., Van Marle, M. J.

1232 E., Morton, D. C., Collatz, G. J., Yokelson, R. J., and Kasibhatla, P. S.: Global fire emissions estimates during 1997–2016,

1233 *Earth Syst. Sci. Data*, 9, 697–720, <https://doi.org/10.5194/essd-9-697-2017>, 2017.

1234 Van Wees, D., Van Der Werf, G. R., Randerson, J. T., Rogers, B. M., Chen, Y., Veraverbeke, S., Giglio, L., and Morton, D.

1235 C.: Global biomass burning fuel consumption and emissions at 500 m spatial resolution based on the Global Fire Emissions

1236 Database (GFED), *Geosci. Model Dev.*, 15, 8411–8437, <https://doi.org/10.5194/gmd-15-8411-2022>, 2022.

1237 Vanguelova, E. I., Bonifacio, E., De Vos, B., Hoosbeek, M. R., Berger, T. W., Vesterdal, L., Armolaitis, K., Celi, L., Dinca,

1238 L., Kjønaas, O. J., Pavlenda, P., Pumpanen, J., Püttsepp, Ü., Reidy, B., Simončič, P., Tobin, B., and Zhiyanski, M.: Sources

1239 of errors and uncertainties in the assessment of forest soil carbon stocks at different scales—review and recommendations,  
1240 *Environ. Monit. Assess.*, 188, 630, <https://doi.org/10.1007/s10661-016-5608-5>, 2016.

1241 Varner, J. M., Kane, J. M., Kreye, J. K., and Engber, E.: The Flammability of Forest and Woodland Litter: a Synthesis, *Curr.*  
1242 *For. Rep.*, 1, 91–99, <https://doi.org/10.1007/s40725-015-0012-x>, 2015.

1243 Veraverbeke, S., Sedano, F., Hook, S. J., Randerson, J. T., Jin, Y., and Rogers, B. M.: Mapping the daily progression of  
1244 large wildland fires using MODIS active fire data, *Int. J. Wildland Fire*, 23, 655, <https://doi.org/10.1071/WF13015>, 2014.

1245 Veraverbeke, S., Dennison, P., Gitas, I., Hulley, G., Kalashnikova, O., Katagis, T., Kuai, L., Meng, R., Roberts, D., and  
1246 Stavros, N.: Hyperspectral remote sensing of fire: State-of-the-art and future perspectives, *Remote Sens. Environ.*, 216, 105–  
1247 121, <https://doi.org/10.1016/j.rse.2018.06.020>, 2018.

1248 Verger, A., Baret, F., Weiss, M., and Weiss, M.: Near real-time vegetation monitoring at global scale., *IEEE J. Sel. Top.*  
1249 *Appl. Earth Obs. Remote Sens.*, 7, 3473–3481, <https://doi.org/10.1109/JSTARS.2014.2328632>, 2014.

1250 Vernooij, R., Giongo, M., Borges, M. A., Costa, M. M., Barradas, A. C. S., and Van Der Werf, G. R.: Intraseasonal  
1251 variability of greenhouse gas emission factors from biomass burning in the Brazilian Cerrado, *Biogeosciences*, 18, 1375–  
1252 1393, <https://doi.org/10.5194/bg-18-1375-2021>, 2021.

1253 Vernooij, R., Winiger, P., Wooster, M., Strydom, T., Poulain, L., Dusek, U., Grosvenor, M., Roberts, G. J., Schutgens, N.,  
1254 and Van Der Werf, G. R.: A quadcopter unmanned aerial system (UAS)-based methodology for measuring biomass burning  
1255 emission factors, *Atmospheric Meas. Tech.*, 15, 4271–4294, <https://doi.org/10.5194/amt-15-4271-2022>, 2022.

1256 Walker, X. J., Rogers, B. M., Veraverbeke, S., Johnstone, J. F., Baltzer, J. L., Barrett, K., Bourgeau-Chavez, L., Day, N. J.,  
1257 De Groot, W. J., Dieleman, C. M., Goetz, S., Hoy, E., Jenkins, L. K., Kane, E. S., Parisien, M.-A., Potter, S., Schuur, E. A.  
1258 G., Turetsky, M., Whitman, E., and Mack, M. C.: Fuel availability not fire weather controls boreal wildfire severity and  
1259 carbon emissions, *Nat. Clim. Change*, 10, 1130–1136, <https://doi.org/10.1038/s41558-020-00920-8>, 2020.

1260 Watts, A. C. and Kobziar, L. N.: Smoldering Combustion and Ground Fires: Ecological Effects and Multi-Scale  
1261 Significance, *Fire Ecol.*, 9, 124–132, <https://doi.org/10.4996/fireecology.0901124>, 2013.

1262 Wiedinmyer, C., Kimura, Y., McDonald-Buller, E. C., Emmons, L. K., Buchholz, R. R., Tang, W., Seto, K., Joseph, M. B.,  
1263 Barsanti, K. C., Carlton, A. G., and Yokelson, R.: The Fire Inventory from NCAR version 2.5: an updated global fire  
1264 emissions model for climate and chemistry applications, *Atmospheric sciences*, <https://doi.org/10.5194/egusphere-2023-124>,  
1265 2023.

1266 Wiggins, E. B., Andrews, A., Sweeney, C., Miller, J. B., Miller, C. E., Veraverbeke, S., Commane, R., Wofsy, S.,  
1267 Henderson, J. M., and Randerson, J. T.: Boreal forest fire CO and CH<sub>4</sub> emission factors derived from tower observations in  
1268 Alaska during the extreme fire season of 2015, *Atmospheric Chem. Phys.*, 21, 8557–8574, <https://doi.org/10.5194/acp-21-8557-2021>, 2021.

1270 Wooster, M. J., Roberts, G., Perry, G. L. W., and Kaufman, Y. J.: Retrieval of biomass combustion rates and totals from fire  
1271 radiative power observations: FRP derivation and calibration relationships between biomass consumption and fire radiative  
1272 energy release, *J. Geophys. Res.*, 110, D24311, <https://doi.org/10.1029/2005JD006318>, 2005.

1273 Wooster, M. J., Freeborn, P. H., Archibald, S., Oppenheimer, C., Roberts, G. J., Smith, T. E. L., Govender, N., Burton, M.,  
1274 and Palumbo, I.: Field determination of biomass burning emission ratios and factors via open-path FTIR spectroscopy and  
1275 fire radiative power assessment: headfire, backfire and residual smoldering combustion in African savannahs, *Atmospheric*  
1276 *Chem. Phys.*, 11, 11591–11615, <https://doi.org/10.5194/acp-11-11591-2011>, 2011.

1277 Wooster, M. J., Roberts, G. J., Giglio, L., Roy, D. P., Freeborn, P. H., Boschetti, L., Justice, C., Ichoku, C., Schroeder, W.,  
1278 Davies, D., Smith, A. M. S., Setzer, A., Csiszar, I., Strydom, T., Frost, P., Zhang, T., Xu, W., De Jong, M. C., Johnston, J.  
1279 M., Ellison, L., Vadrevu, K., Sparks, A. M., Nguyen, H., McCarty, J., Tanpipat, V., Schmidt, C., and San-Miguel-Ayanz, J.:  
1280 Satellite remote sensing of active fires: History and current status, applications and future requirements, *Remote Sens.*  
1281 *Environ.*, 267, 112694, <https://doi.org/10.1016/j.rse.2021.112694>, 2021.

1282 Wu, M., Knorr, W., Thonicke, K., Schurgers, G., Camia, A., and Arneth, A.: Sensitivity of burned area in Europe to climate  
1283 change, atmospheric CO<sub>2</sub> levels, and demography: A comparison of two fire-vegetation models, *J. Geophys. Res.*  
1284 *Biogeosciences*, 120, 2256–2272, <https://doi.org/10.1002/2015JG003036>, 2015.

1285 Xiang, D., Wang, G., Tian, J., and Li, W.: Global patterns and edaphic-climatic controls of soil carbon decomposition  
1286 kinetics predicted from incubation experiments, *Nat. Commun.*, 14, 2171, <https://doi.org/10.1038/s41467-023-37900-3>,  
1287 2023.

1288 Xifré-Salvadó, M. À., Prat-Guitart, N., Francos, M., Úbeda, X., and Castellnou, M.: Smoldering Combustion Dynamics of

1289 a Soil from a *Pinus halepensis* Mill. Forest. A Case Study of the Rocallaura Fires in Northeastern Spain, *Appl. Sci.*, 10,  
1290 3449, <https://doi.org/10.3390/app10103449>, 2020.

1291 Yigini, Y. and Panagos, P.: Assessment of soil organic carbon stocks under future climate and land cover changes in Europe,  
1292 *Sci. Total Environ.*, 557–558, 838–850, <https://doi.org/10.1016/j.scitotenv.2016.03.085>, 2016.

1293 Yilmaz, O. S., Acar, U., Sanli, F. B., Gulgen, F., and Ates, A. M.: Mapping burn severity and monitoring CO content in  
1294 Türkiye’s 2021 Wildfires, using Sentinel-2 and Sentinel-5P satellite data on the GEE platform, *Earth Sci. Inform.*, 16, 221–  
1295 240, <https://doi.org/10.1007/s12145-023-00933-9>, 2023.

1296 Yokelson, R. J., Griffith, D. W. T., and Ward, D. E.: Open-path Fourier transform infrared studies of large-scale laboratory  
1297 biomass fires, *J. Geophys. Res. Atmospheres*, 101, 21067–21080, <https://doi.org/10.1029/96JD01800>, 1996.

1298 Zheng, B., Chevallier, F., Ciais, P., Yin, Y., and Wang, Y.: On the Role of the Flaming to Smoldering Transition in the  
1299 Seasonal Cycle of African Fire Emissions, *Geophys. Res. Lett.*, 45, 11,998–12,007, <https://doi.org/10.1029/2018GL079092>,  
1300 2018.

1301 Zhou, D. K., Larar, A. M., Liu, X., and Xiong, X.: Estimation of fire-induced CO plume age from NAST–I during the  
1302 FIREX-AQ field campaign, *J. Appl. Remote Sens.*, 16, <https://doi.org/10.1117/1.JRS.16.034522>, 2022.

1303 Zin, E., Kuberski, Ł., Drobyshev, I., and Niklasson, M.: First Spatial Reconstruction of Past Fires in Temperate Europe  
1304 Suggests Large Variability of Fire Sizes and an Important Role of Human-Related Ignitions, *Front. Ecol. Evol.*, 10, 768464,  
1305 <https://doi.org/10.3389/fevo.2022.768464>, 2022.